processes

MDPI

Review

Photochemical Catalysts for Hydrocarbons and Biomass Derivates Reforming in Intensified Processes

Mattia Boscherini and Francesco Miccio *

National Research Council−Institute of Science, Technology and Sustainability for Ceramics (CNR−ISSMC), Via Granarolo 64, 48018 Faenza, Italy; mattia.boscherini@cnr.it
* Correspondence: francesco.miccio@cnr.it

Abstract

Photocatalysts for applications in different sectors, e.g., civil and environmental, are already developed to a mature extent and allow, for example, the purification of gaseous and liquid streams or the self−cleaning surfaces. The application of photocatalysts in the industrial sector is, however, quite limited. The review addresses the specific topic of the photocatalytic reforming of methane and biomass derivates. In this regard, recent advances in materials science are reported and discussed, in particular regarding doped and modified oxides (TiO_2 and ZrO_2) or non−oxidic ceramics. Concerning process integration, a comparison between traditional two−dimensional photoreactors and fluidized bed systems is proposed and design guidelines are drawn, with indications of the possible benefits. Photocatalytic fluidized beds appear more suitable for small− and medium−scale integrated processes of reforming, operating at lower temperatures than traditional ones for distributed hydrogen generation.

Keywords: photocatalysis; reforming; partial oxidation; tar abatement; fluidized bed

Academic Editor: Renquan Guan

Received: 9 June 2025
Revised: 1 July 2025
Accepted: 3 July 2025
Published: 6 July 2025

Citation: Boscherini, M.; Miccio, F. Photochemical Catalysts for Hydrocarbons and Biomass Derivates Reforming in Intensified Processes. *Processes* **2025**, *13*, 2150. https://doi.org/10.3390/pr13072150

1. Introduction

As the principal pathway for hydrogen and syngas production, hydrocarbon reforming is one of the most important processes of the chemical industry. More than 40% of the world's hydrogen production is obtained through steam reforming of natural gas, and the hydrogen and syngas demands are expected to be ever increasing in the next future [1]. However, the conventional steam reforming reaction, typically performed on methane (R1), is highly endothermic and requires the use of a catalyst, high temperatures, and high amounts of excess water compared to stoichiometry to obtain suitable yields and limit side reactions, such as methane cracking (R2), which result in coke deposition on the catalyst's surface [2,3].

$$CH_{4(g)} + H_2O_{(g)} \rightleftharpoons CO_{(g)} + 3H_{2(g)} \qquad \Delta H^\circ = 204\ kJ/mol \qquad (R1)$$

$$CH_{4(g)} \rightarrow C_{(s)} + 2H_{2(g)} \qquad \Delta H^\circ = 74\ kJ/mol \qquad (R2)$$

The high reaction temperature required results in a very energy intensive process, and while noble metal−based catalysts would be able to provide very good yields and high reaction selectivity towards syngas production with limited coke formation, they are too expensive to be commercially used, with nickel−based catalysts being the industry standard in modern processes instead [4,5]. However, nickel is a toxic metal [6], leading to safety problems when handling catalysts and during disposal. Coke formation and sulfur

poisoning become particularly relevant problems when considering biogas dry reforming, which would otherwise be a much more sustainable process compared to steam reforming of natural gas, being potentially able to achieve negative carbon dioxide emissions [7]. Biogas usually contains high concentrations of carbon dioxide in addition to methane; therefore, the direct application of a dry reforming reaction (R3) would allow methane conversion without expensive separation pre−treatments [8]. Unfortunately, dry reforming is an even more endothermic reaction which is also much more affected by coke deposition compared to steam reforming, as CO_2 is a weaker oxidant, with the Boudouard reaction (R4) and reverse water–gas shift reactions (R5) negatively affecting yield and H_2/CO ratio [9,10].

$$CH_{4(g)} + CO_{2(g)} \rightleftharpoons 2CO_{(g)} + 2H_{2(g)} \quad \Delta H^\circ = 247\ kJ/mol \quad (R3)$$

$$2CO_{(g)} \rightleftharpoons C_{(s)} + CO_{2(g)} \quad \Delta H^\circ = 172\ kJ/mol \quad (R4)$$

$$CO_{2(g)} + H_{2(g)} \rightleftharpoons CO_{(g)} + H_2O_{(g)} \quad \Delta H^\circ = 41\ kJ/mol \quad (R5)$$

It should be noted that compared to the steam reforming reaction, dry reforming also has the distinction of obtaining a lower H_2 to CO ratio, which is useful for obtaining syngas, which can be directly used in chemical synthesis without post−treatments. The steam and dry reforming reactions can finally also be applied to higher hydrocarbons and are, for example, also utilized for the abatement of tar from biomass gasification [11–13]; however, the high temperature requirements of the reaction and the subsequent deactivation of catalysts due to sintering and coke deposition remain great issues in the implementation of the process. Several alternatives in terms of catalyst support, dopants, promoters, and structure have, thus, been investigated to improve reactant conversion and limit poisoning [14–22]. In recent years, interest in alternatives to conventional thermochemical processes, such as plasma reforming [23], electrochemical reforming [24], and photocatalytic reforming [25], has also significantly grown, as briefly reported in Figure 1. In conventional thermochemical processes (Figure 1a), the energy required for the reaction is provided in the form of heat by operating at a high reaction temperature. On the other hand, the alternative processes employ a variety of strategies to decrease the temperature of operation: plasma reforming (Figure 1b) utilizes high−voltage electrodes integrated in the reactor design to produce an electrical discharge in the gas phase that causes the formation of plasma with a high electron temperature, which then activates methane and oxidant molecules by forming radical and ionized species which then interact over the catalyst surface [26,27]. Electrochemical processes (Figure 1c) also use electrical current and difference in electrical potential to provide the oxidation of methane and the reduction of the oxidant over the electrodes of a liquid phase or solid phase fuel cell, but they do not involve the formation of plasma and the charge is instead transferred through the diffusion of ions in a liquid or solid media between electrodes. Finally, photochemical processes (Figure 1d) make use of light to provide the energy required for reactant activation. Photocatalytic processes, in particular, can provide very eco−friendly pathways for chemical conversion, especially if directly driven by sunlight [28], and, in recent years, have been studied for a vast number of applications, ranging from wastewater treatment [29] to chemical synthesis [30]. The use of photocatalysis can enable forming reactions in much milder conditions compared to conventional thermochemical processes, lowering CO_2 emissions and limiting problems, such as catalyst sintering [31]. Compared to conventional thermal processes and to electrochemical processes, the photocatalytic approach has the fundamental advantage that, through the activation of chemical bonds by photoexcited electrons, it is possible to drive uphill reactions against thermodynamic restrictions, as the mechanism of reaction is completely changed, allowing researchers to potentially bypass thermodynamic equilibri-

ums [28,32,33]. This advantage is shared with the plasma−reforming processes, where the excited electrons of the non−thermal plasma can also activate chemical bonds; however, photocatalysis has the advantage of not requiring plasma generation, which is an energy intensive process [34–36].

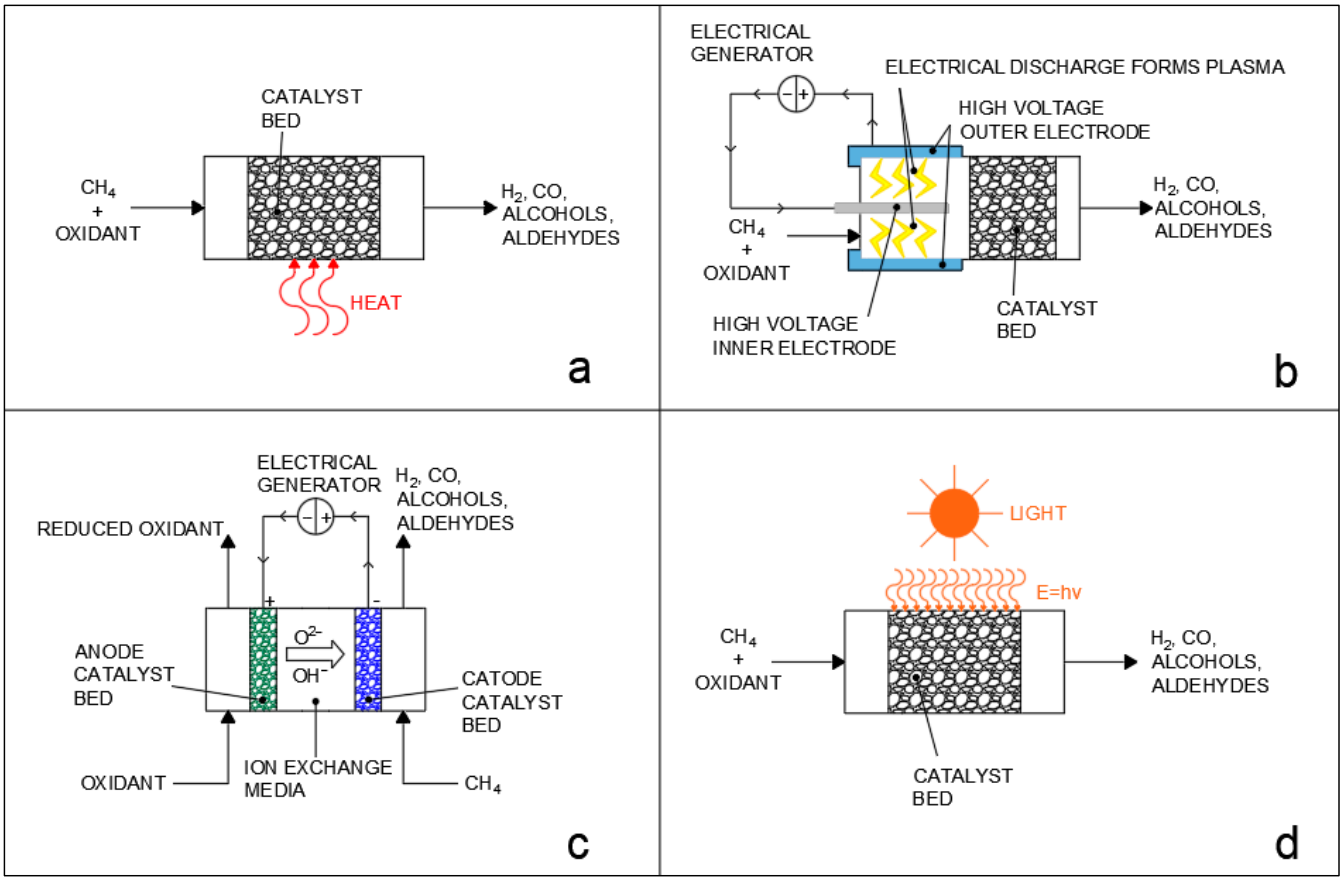

Figure 1. Different approaches to methane/hydrocarbon reforming: (**a**) thermocatalytic reforming; (**b**) plasmacatalytic reforming; (**c**) electrocatalytic reforming; (**d**) photocatalytic reforming. Oxidants may be either oxygen (partial oxidation), steam (steam reforming), or carbon dioxide (dry reforming).

One of the most crucial aspects of photocatalysis is, thus, the selection of photocatalysts, which determines the effectiveness of light (LT) utilization through the induction of electrons and charge transfers when exposed to light [37,38]. In the last few years, significant effort has been dedicated to the enhancement of activity of semiconductor photocatalysts for photo−reforming processes by surface and nanostructure engineering, doping, and the utilization of cocatalysts. Previous reviews have been published on the state of the art of the photo−reforming process: Li et al. 2021 [39] and Song and Ye 2022 [40] both reviewed the state of the art of photocatalytic methane conversion, pointing out that the selection of the photocatalyst and the determination of the photocatalytic mechanism are the current bottlenecks of further process development. Recently, Cho et al. [41] provided a detailed review of photocatalysis for methane partial oxidation, steam, and dry reforming, pointing out specifics about reaction mechanisms and requirements for methane activation. Kulandaivalu et al. [42] instead reviewed in greater detail the photocatalytic dry reforming of methane: they noted that for the proper advancement of the process, there is a need to produce novel catalysts able to activate methane as well as carbon dioxide, which are currently lacking in the literature. It should be noted that several of the studied photocatalyst involve the use of expensive noble metal photocatalysts, which would greatly limit the viability of such processes on a large−scale application. Reviews by Liu et al. [25] and Wang

et al. [43] discussed the state of the art of semiconductor−based photocatalysts, highlighting the main pathways available for catalyst improvement, such as surface engineering and use of dopants, electron scavengers, and cocatalysts: so far, modified TiO_2, ZrO_2, WO_3, and C_3N_4 have been the most tested photocatalysts. The most recent review by Lei et al. [44] highlights that the study and development of catalysts with a ferroelectric effect may allow researchers to increase catalytic performances. As per the photocatalytic reforming of biomass, recent reviews were provided by Xu et al. [45] and Pan et al. [46]. On the other hand, to the authors' knowledge, no comprehensive reviews have been published on the use of photocatalysis for tar reforming and abatement. As an alternative to conventional semiconductors, novel covalent organic framework (COF) catalysts have also been proposed [47] but are still in their infancy and suffer from slow preparation, limited versatility in structure modification, and limited efficiency. On the other hand, the development of quantum dots [48,49] and heterojunction−based semiconductor composites [50] could offer great promise in advancing conventional semiconductor materials.

In addition to photocatalyst selection, reaction conditions, such as the selected light source, reaction media, and temperature, as well as reactor design, also play a crucial role in determining process performance. In their reviews, Liu et al. [25] and Wang et al. [43] also briefly discussed the current state of the art of reactor designs for aqueous phase methane conversion. A more extensive discussion on batch and flow reactor designs was presented by Jiang et al. [51], who provided a selection of guidelines for homogenizing experimental practices and comparison of data results to focus on the most promising technologies. Compared to conventional thermal reactors, photoreactors generally face less extreme conditions in terms of reaction temperature and pressure, with their main design challenges instead being the need to properly design the fluid dynamics and the light generation and distribution system [52,53], which are essential to ensure optimal mass transfer and effective light utilization. In the case of aqueous phase reactions, pH and corrosion need to be also accounted for [54,55], as the photocatalytic reaction may require alkaline or acidic environments. The optimization of photocatalytic reactors is, thus, still an open field of investigation.

Finally, the coupling of thermocatalytic and photocatalytic processes, as well as coupled plasma–photocatalytic processes, has also been reported as another interesting perspective to enhance productivity for reforming reactions [56,57].

Despite the increasing effort that photocatalytic reforming has been receiving in the literature, an optimized photocatalytic reforming process is still lacking thus far. Great effort has been dedicated to the reforming of methanol and aqueous organic species, with methane photocatalytic reforming receiving more limited studies, with a great number of available works involving the use of expensive noble metals or toxic species, such as nickel. While solar photocatalytic reforming could allow for substantial reduction in the environmental impact, further improvements in reactor design and catalytic activity are still required [58]. Since photocatalysis is a rapidly growing field, there is a need for frequent reporting of up−to−date information. Thus, this review expands on the previously published literature, with the goal of highlighting new technological developments and strategies to design intensified photocatalytic processes, in particular by adopting fluidized bed (FB) technology.

2. Catalysts for Photoconversion

2.1. General Mechanism of Photocatalysis and Photocatalyst Engineering

An example of a typical photocatalytic mechanism [59,60] for organic compound photooxidation on a semiconductor catalyst is shown in Figure 2.

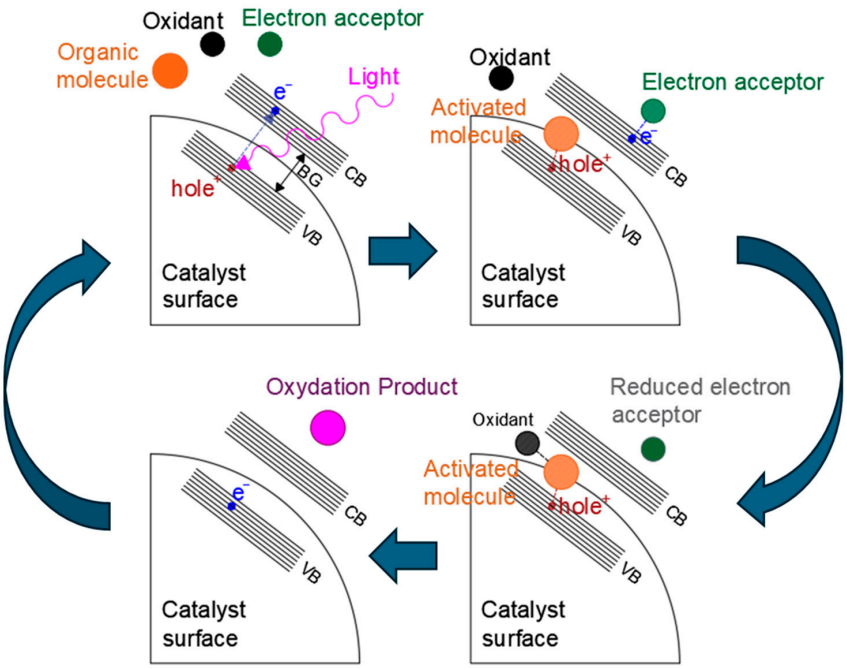

Figure 2. Example of a photocatalytic reaction mechanism. VB = valence band, CB = conduction band, and BG = band gap.

Generally speaking, the reaction starts with the light−induced excitation of an electron in the valence band of the photocatalyst. The excited electron is promoted to the valence band, leaving a positively charged hole in the conduction band. At this point, the electron can either recombine with the hole and re−emit the captured photon, thus resulting in a zero net−reaction, or it can be transported through the valence band, where it is then captured by an electron acceptor found in the reaction media. At the same time, the valence band hole interacts with the organic molecule, intercepting the electrons of its orbitals (for example the electrons of C−H bonds). The organic molecule is, thus, activated, allowing its reaction with the oxidant and leading to the formation of products and the restoration of the catalyst valence band by the filling of the electron hole due to electron donation, which can be followed by further electron excitation as a new photon is captured, starting the cycle again. Optimization of the band gap energy [61], inhibition of excessive hole–electron recombination [62], distribution and interaction of valence band holes, and conduction bands electrons with organic donors and acceptors [63,64] are, thus, essential aspects of photocatalyst design. In recent years, different approaches have been proposed to optimize activity of semiconductor heterogeneous catalysts. For example, the inclusion of metal and non−metal dopant atoms can induce the formation of localized intermediate energy levels between the conduction and valence bands of the photocatalyst [65,66], which lowers the energy required for electron transitions and widens the radiation spectra that is usable by the material, expanding it to higher wavelengths. Similar effects may also be obtained by defect and surface structure engineering [67,68], and particularly by producing nano−structured photocatalysts [69–71] (i.e., nanospheres, nanorods, 2D nanosheets, nanopores, nanotubes, etc.), where the incomplete coordination of atoms in surface and defect sites also causes the formation of energy levels that can act as charge separators, electron traps, or charge recombination sites. Loaded metal species on the catalyst surface demonstrate effective improvement of photocatalyst activity by capturing electrons and reducing charge recombination, as well as improving charge transfer [72,73]. Finally, in the last years, the study of more complex structures, such as quantum dots and heterojunction structures, has also shown promising results. Heterojunctions are formed at

the interface by the mixture of different semiconductor materials with an unequal band structure, or at the interface between semiconductors and metals [74]: in these areas, the interaction of the two phases can induce alteration of the energy levels and create an electrical field that enhances charge separation. Heterojunctions between semiconductor surfaces can be distinguished as being type I, type II, type III, S−scheme, or Z−scheme [75], as shown in Figure 3. In type I heterojunctions, also called a "straddling gap heterojunction", the valence and conduction bands of one of the semiconductors are located in between those of the other. In type 2 heterojunctions, called also "staggered gap" heterojunctions, the VB and CB of one of the catalysts are both higher than the respective bands of the other. Type 3 heterojunctions ("broken gap"), on the other hand, have one of the photocatalyst possess both a VB and CB higher than the other catalyst's CB. Heterojunctions of the p−n type form at the interface between n− and p−types semiconductors, where the diffusion of electrons from the p−type semiconductor to the n−type one and the counter diffusion of holes from n−type to p−type occurs even before light exposure, leading to the formation of an internal electrical field at the interface that favors electron–hole separation once the material is excited by light. S−scheme heterojunctions (sometimes indicated as direct Z−scheme heterojunctions) are similar to type II, presenting a staggered band gap, but the electron transfer happens between the conduction band of a catalyst to the valence band of the other [76]. Finally, in Z−scheme heterojunctions, the electron transfer is mediated by an intermediate species that acts as an electron carrier [77]. Z−scheme heterojunctions may involve dissolved species in a solution as the electron mediator, or they can involve solid phase mediators. Another type of heterojunction, called a Schottky barrier heterojunction [78], is formed at the interface between a semiconductor and a conductor material, such as a metal, with electrons migrating towards the more conductive material and forming a potential energy barrier that inhibits their back diffusion, thus trapping them on the conductive species.

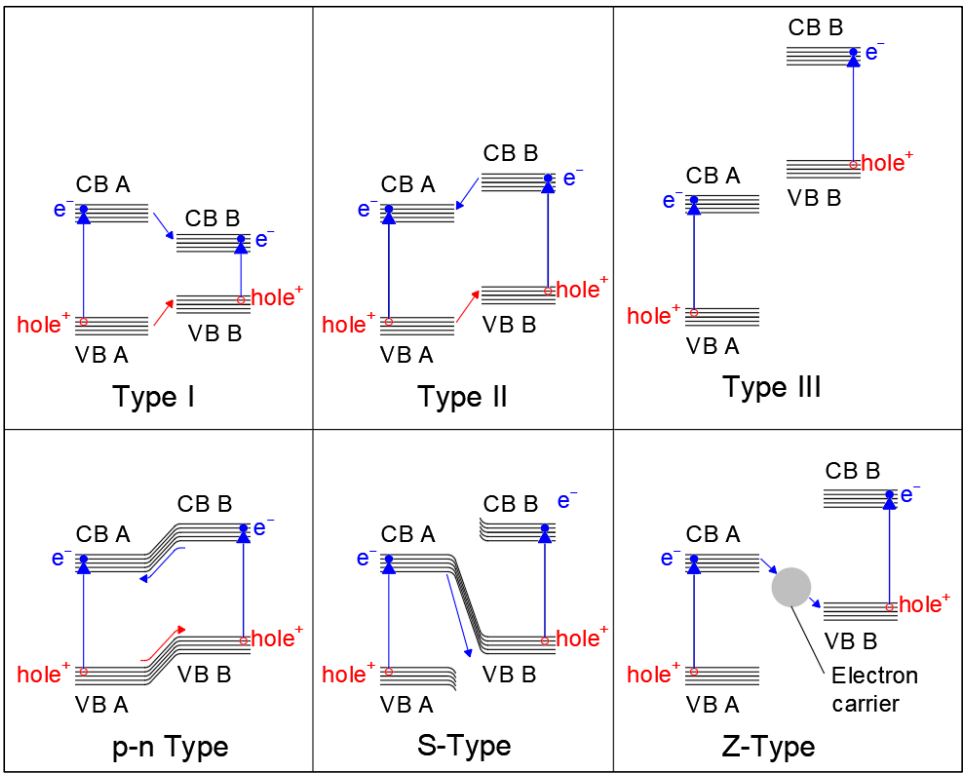

Figure 3. Types of heterojunction structures. Blue lines indicate electron transfer; red lines indicate hole migration.

The type of heterojunction strongly affects the activity of the photocatalyst: type 1 and 3 heterojunctions, for example, cannot inhibit electron–hole recombination, since in the former, both electron and holes tend to migrate in the same direction, while in the latter, diffusion of both electrons and holes is inhibited by the band gap incompatibility of the semiconductors. Thus, type 2, S−scheme, Z−scheme, and p−n type band gaps are the most relevant for photocatalytic applications, with S−scheme and Z−scheme materials attracting much interest due to their superior charge separation ability.

Finally, quantum dots are formed when materials are deposited in near zero−dimensional nanostructures with a radius inferior to the radius of the material's excitons (excited hole–electron pairs) [79,80]; in these conditions, the band gap of the material becomes size−dependent, offering great tunability of light absorption and activity under visible light, and, due to quantum confinement effects, the number of excitons generated is increased compared to bulk materials.

2.2. TiO_2−Based Catalysts

Among various materials, titanium oxide is a typical choice for photocatalytic processes due to its high activity, good thermal and chemical stability, low cost, and non−toxicity [81]. Unfortunately, titanium oxide on its own is only active under ultraviolet (UV) radiation [82,83], which is only a small fraction of sunlight (3–5%) [60], thus leaving most of the solar spectrum unused and limiting process efficiency. Conventional mercury−based UV lamps pose safety and environmental problems due to the high toxicity of mercury, while they provide a limited light production efficiency with a short lifespan [84]. On the other hand, it should be noted that while the direct use of sunlight is a most desirable outcome, in the last few years, UV technology has also made substantial progress, which can offer the opportunity of efficiently employing UV in photocatalytic processes, thanks to the replacement of conventional mercury lamps with more efficient systems, such as excimer lamps or light−emission diodes (LEDs) [84–87]. Nevertheless, substantial effort has been dedicated in the last few years to expand TiO_2 photocatalytic activity to the vs., including via surface treatments and functionalization, formation processes, inclusion in composite materials, use of organic and inorganic promoters, and doping of the titania structure with metals and non−metals [88–94]. In particular, doping titanium oxide and the subsequent formation of lattice defects can introduce intermediate electron levels between the valence and conduction bands and widen the respective bands themselves, thus lowering the band gap and allowing electron excitation and conduction even under the longer wavelengths of visible (VS) and infrared light (IR) [95]. When considering metal promoters and dopants, the addition of noble metals has been shown to significantly enhance TiO_2 photocatalytic activity [96,97]; however, their high cost makes their use unfeasible for large scale operation. Among non−noble metals, both transition metals, such as Ni [98,99], Fe [100,101], Cu [102,103], Co [104], and Mn [105,106], and rare earths, such as Ce [107] and La [108], have all been found to effectively improve photocatalytic activity when used as dopants. While a significant number of the studies on TiO_2 photocatalysis focus on the degradation of organic pollutants, typically in an aqueous environment, photocatalytic reforming and hydrogen production from methane and biomass derivatives have also attracted interest.

Noble metals, and in particular Pt, are able to increase TiO_2 activity for the reforming of methane, biomass derivates, and tar compounds: Yamaguchi et al. [109] observed enhanced performance for steam methane reforming using TiO_2 hollow spheres with spatially separated Pt−Rh noble metal cocatalysts: they proposed that in their hollow TiO_2 sphere structure the excited electrons of the TiO_2 could be transferred to Pt particles loaded in their internal surface, where they then produced hydrogen by water reduction, while the electron

holes migrated to the Rh_2O_3 oxide layer deposited on the external surface, where they oxidized methane. This mechanism provided an effective charge separation not only by band gap energy, but also by spatial separation of the electron sink and hole sink materials. On the other hand, Al−Madanat et al. [110] investigated the mechanism of naphthalene aqueous phase reforming for hydrogen formation over Pt−loaded TiO_2, concluding that water is the source of both hydrogen and oxygen. During naphthalene mineralization to CO_2 Pt atoms again act as an electron sink and site for the reduction. Naphthalene is primarily activated through the formation of naphthalene cation radicals. The use of a Pt cocatalyst in conjunction with hydrothermally prepared Nb_2O_5−TiO_2 photocatalysts proved effective for the photoreforming of ethanol aqueous solutions to hydrogen [111], obtaining an apparent quantum yield of 85% under simulated sunlight; the best results were observed for a composite that underwent 3 days of hydrothermal treatment, which outperformed pure P25 TiO_2 catalyst, but in this case no direct investigation of the mechanism was performed, though the authors proposed that the formation of favorable type II and S−scheme heterojunctions is the cause of improved performance for this composite.

The use of nickel has been commonly investigated as an alternative to noble metals. Glycerol photoreforming was investigated by Eisapour et al. [112], who obtained a remarkable 58% glycerol conversion to hydrogen and value−added glyceraldehyde and dihydroxyacetone using a NiO−Ni−TiO_2 sandwich−like heterojunction catalyst, bypassing the limitations of single p−n heterojunction catalysts. Glycerol was converted to glycerate through the formation of glyceraldehyde and to ketomalonate through the formation of hydroxyacetone and hydroxypiruvate. They proposed that the p−n heterojunction formed between NiO and TiO_2 interfaces favored the initial separation of electron–hole pairs, and then the metallic Ni species further captured electrons from TiO_2 by forming a Schottky heterojunction, thus acting as a barrier for charge recombination and functioning as a center for hydrogen production, while electron holes were transferred to the NiO surface and oxidized the organic substrate. On the other hand, Liu et al. [113] obtained a 96.1% selectivity towards syngas formation from glycerol by engineering Ni−O−Ni dimer sites in a TiO_2−derived metal–organic framework (MOF) structure. Single Ni atom deposition reduces the contact angle between TiO_2 and substrate species, favoring their adsorption on the catalyst surface. The electrons of NiO_2 dimers are rapidly redistributed on the TiO_2 surface, where they are used to produce hydrogen, and the formed holes in dimer sites adsorb and activate glycerol, oxidizing it through the formation of formaldehyde and formic acid intermediates. The porosity and structure of the TiO_2 support also contribute to catalytic activity: Xie et al. [114] obtained improved performances for methane dry reforming by depositing Ni on mesoporous TiO_2, while He et al. [115] observed the remarkable effects of the TiO_2 crystal phase for Ni/TiO_2 photocatalysts, with an optimized rutile to anatase ratio leading to better exposed Ni species and remarkable H_2 and CO production rates reaching 87.4 and 220.2 mmol/(g·h), respectively. While the use of nickel is problematic from an environmental perspective, these studies still demonstrate the remarkable effect of catalyst structure engineering on activity and selectivity.

Copper addition may provide an effective alternative to Ni in preparing more active photocatalysts. For example, the sequential deposition of NiCu catalyst over P25 TiO_2 was observed to be effective for the conversion of cellulose to hydrogen and organic acids, with a H_2 yield of 489 μmol/(g·h) for a 1% wt. CuNi−loaded catalyst [116]: sequential deposition of Ni followed by Cu led to a more active catalyst compared to a catalyst produced by simultaneous co−deposition, suggesting improved interaction between metal species, and a low loading was sufficient to enhance activity without incurring deactivation due to excessive TiO_2 site covering observed at higher metal loading, at the same time allowing the reduction in Ni loading. Ni and Cu species were proposed to form Schottky

heterojunctions with the TiO_2 surface, acting as electron accumulation and hydrogen generation sites. Aside from the cleavage and oxidation of cellulose by electron holes on the catalyst surface, side reactions of transposition, hydrolysis, and decarboxylation are expected to occur, leading to the formation of subproducts, such as glucose, cellobiose, mannose, maltose, acetic and formic acids, and other. As per pure copper−modified TiO_2−based catalysts, Clarizia et al. [103] provided a review on the aqueous reforming of organic species and observed a great scarcity of hydrogen production efficiency data for such processes. More recently, Muscetta et al. [117] observed a promising performance for aqueous phase reforming of biomass derivates using a ball−milling−prepared Cu_2O−TiO_2 photocatalyst: they observed that a 1% wt. addition of Cu_2O resulted in nearly 60% of the hydrogen yield obtained under sunlight being derived from visible light absorption. The reaction rate could be described by the Langmuir–Hinshelwood model, and it was favored at alkaline pH and a temperature increase from 20 °C to 80 °C. Glycerol and ethylene glycol were the best substrates in terms of hydrogen yield, followed by methanol. Negligible yield was obtained from lactic and formic acid instead, attributed to limits in substrate adsorption on the catalyst surface and the reduced stability of copper species in acidic conditions. They proposed that the reaction mechanism involves the formation of a p−n heterojunction between Cu_2O and TiO_2 surfaces, where Cu_2O can absorb visible sunlight and then transfer electrons to the TiO_2 support. Umair et al. [118] tested a similar catalyst in a 10 L pilot−scale reactor for hydrogen production from biomass derivatives, such as glycerol, ethanol, and glucose, obtaining remarkable hydrogen yields for a 3% wt. Cu_2O−loaded sample ball milled at 150 rpm for 2 h. The addition of Cu_2O effectively shifted the catalyst band gap in the vs. light range, improving light utilization, and the best hydrogen yield was observed for degradation of glycerol. They also supported a mechanism involving the formation of a p−n heterojunction that favors electron–hole separation, where Cu_2O acts as the species active to visible light absorption, with electrons being separated over TiO_2. This represents one of the first efforts to implement photocatalytic hydrogen production on a pilot scale. Khan et al. [119] recently observed high activity for H_2 production from methanol coupled with CO_2 reduction on MOF−structured Cu−TiO_2 composite catalysts, for the first time surpassing the performance of a reference 1% w, Pt−TiO_2 composite after three photocatalytic reaction cycles: the MOF structure highly enhanced catalyst performance compared to simple Cu deposition at the same load, and hydrogen yield improved over subsequent reaction cycles, reaching 13.24 mmol/(g·h) after six cycles. Copper was initially present mainly in the +1 oxidation state in the catalyst, with some metallic Cu nanoclusters also being present, and was reduced to metallic Cu during the reaction. The formation of stable metallic Cu nanoclusters in the MOF structure was credited with the increased catalytic performance of the composite material. The MOF structure prevents aggregation of the nanoclusters and limits their back oxidation, improving catalyst stability. A Schottky heterojunction is formed between these metal nanoclusters and the TiO_2 surface, acting as electron sink which prevents improved charge separation. Carboxylic groups are a fundamental intermediate in the reaction mechanism. The effects of Cu oxidation state on H_2 production from methanol and CO_2 reduction to methane were investigated by Qian et al. [120]: the bandgap of the copper–titania heterojunction catalysts narrowed and the vs. light absorption range significantly broadened with the transition of the Cu valence state from Cu(I) to Cu(0). The more reduced copper species were, thus, found to improve the charge separation of the catalyst and enhance its activity under vs. light. The surface area of the catalyst plays a very significant role in its activity: hydrothermally prepared Cu−TiO_2 samples were found to outperform samples prepared by impregnation [121], even when their oxidation state was unchanged between the two different syntheses; the hydrothermally prepared

sample's increased activity was attributed to improved dispersion of the Cu species and the increased surface area, which favored substrate adsorption and oxidation and decreased the band gap of the photocatalyst due to the better interaction of copper with the TiO_2 substrate. On the other hand, calcination was observed to negatively affect activity, as it reduced the availability of surface copper species. The addition of cerium dioxide together with copper was instead observed by Liu et al. [122], who concluded that a Ti/Ce ratio of 2:1 increases the performance of a Cu/TiO_2-CeO_2 photocatalyst for gas−phase methanol steam reforming, achieving up to 100% methanol conversion and high hydrogen selectivity.

Cobalt is another possible substitute for both Ni and noble metals. A high 95% conversion was observed for reforming glycerol to formic acid and formaldehyde on Co−doped TiO_2 [123]: Co−doping induced lattice strain in TiO_2 and increased the number of oxygen vacancies, which is further increased during light irradiation, providing numerous oxygen adsorption sites; the adsorbed oxygen was reduced to $\bullet O^{2}-$ radicals by electrons concentrated on the Co specie, and these radicals then interacted with the glycerol molecules activated by electron holes, leading to C−C bond cleavage, with the primary oxidation pathway involving glyceraldehyde formation as a reaction intermediate. An S−shaped heterojunction−based 10% wt. $-Co_{0.3}Ni_{0.55}Se/TiO_2$ catalyst achieved a remarkable hydrogen yield of 10,070.9 μmol/(g·h) when degrading 20% vol. triethanolamine (TEOA) aqueous solutions [124]: electrons were concentrated on the CoNiSe clusters and then used to generate hydrogen from H^+ cations, while holes accumulated in the TiO_2 support and oxidized the organic substrate.

Other metals could also provide useful improvements in photocatalyst activity. Ayodele et al. [125] optimized La−doped TiO_2 through the use of response surface methodology and analysis of variance, obtaining a hydrogen yield of 2.43 μmol/min. In their optimization, they evaluated the effect of four different independent variables (irradiating time, metal loading, methane concentration, and steam concentration) on the rate of hydrogen production, obtaining optimum conditions of 146.15 min, 2.94%, 22.83%, and 1.24% for irradiation time, metal loading, methane concentration, and steam concentration, respectively. Unfortunately, they did not investigate the reaction mechanism and the effects of La addition on the band gap. On the other hand, Zhang et al. [126] tested W−doped TiO_2 nanocrystals for the oxidation of ethylbenzene to acetophenone. The presence of the W atoms induces electron transfer from the TiO_2 to W species, while at the same time inducing lattice distortion and the formation of numerous oxygen vacancies; W species then proceed to reduce oxygen to $\bullet O^{2}-$ radicals, while electron holes activate ethylbenzene. The composite material obtained yields 16 times higher than pure TiO_2 in the same reaction conditions. Finally, Hu et al. [127] demonstrated a 1653 μmol/(g·h) hydrogen yield from MoS_2−modified TiO_2 nanoparticles using agricultural biomass substrates. In this case, the conduction band of MoS_2 acted as sink for the electrons generated by the photoexcitation of TiO_2, which then converted H^+ cations to hydrogen, while the holes in the titania valence band converted water to hydroxyl radicals that were then scavenged by the biomass substrate. No hole migration is expected to occur between TiO_2 and MoS_2 species, due to the wide difference in energy between the two materials' valence bands.

Alternatives to metal doping have also been investigated: Falara et al. [128] demonstrated ethanol conversion and H_2 generation on TiO_2 modified by carbon dot deposition, studying quantum dots obtained from hydrothermal treatment of microwave irradiation. They observed a strong dependence of the carbon dots activity on the precursor and methodology, with microwave irradiation−prepared samples outperforming the ones produced by the hydrothermal method. Nitrogen presence in the quantum dots' precursor is proposed to be important to ensure optimal charge separation efficiency, while excessive

quantum dot deposition negatively impacts yield, which was attributed to such phenomena as light scattering recuing the absorption efficiency of light.

Finally, it should be noted that a simple change in catalyst morphology can lead to a very remarkable change in performance even without the presence of dopants or cocatalysts: Ubaidah et al. [129] observed that altering the TiO_2 structure from commercial P25 powder to nanotubes caused the surface area to increase from 55.76 to 120.99 m^2/g, while simultaneously reducing the band gap of the material from 3.32 to 3.23 eV and increasing the CH_4 yield from 6560 to 17,020 μmol/(g·h) under UV−VS light. Compared to nanospheres, where electrons can move from the bulk to the surface of the material, in the nanotubes, the electrons are trapped in a new energy band with a lower energy level, and the alternative scenarios for electron and hole dynamic involve the movement of electrons and holes along the axis of the tube, thus making recombination less likely and improving the electron availability for reaction. Jiang et al. [130] also obtained a selective photocatalyst for the photooxidation of methane to formaldehyde by engineering a TiO_2 crystal structure, demonstrating the possibility of controlling process selectivity through photocatalyst structure, and, in particular, they observed that a 90% anatase–10% rutile phase mixture of TiO_2 was able to provide optimized activity towards methane activation through the formation of an heterojunction between the two different crystal phases, with electrons migrating to the anatase and holes migrating to the rutile. The hybrid crystal structure also demonstrated an improved lifetime. Finally, crystal−phase engineering was also demonstrated to be able to drastically enhance the performance of TiO_2 for catalyzing non−oxidative methane coupling, with biphasic TiO_2 (anatase 30% and rutile 70%) exhibiting the highest photocatalytic activity [131].

Morre novel approaches have also been proposed, such as the coupling of photocatalysis with plasma activation. For example, Sun et al. [132] obtained toluene conversion as high as 98% by coupling microwave plasma−catalyzed steam reforming with photocatalysis by anatase TiO_2 at moderate humidities of 38%. Higher humidities were found to decrease conversion.

The results for TiO_2 photocatalysts are reported in Table 1.

2.3. ZrO_2−Based Catalysts

ZrO_2−based photocatalysts are a common substitute for TiO_2, sharing very similar properties in terms of their low cost and high thermal and chemical stability [133,134]. Unfortunately, they also share the problem of having a large band gap energy, thus being active only under UV light and needing modification to operate under vs. radiation. Metal doping of ZrO_2 has, thus, been extensively investigated to enhance its photocatalytic activity [133]. Aside from noble metals, transition metals are the most studied for the enhancement of ZrO_2's performance, with a great number of recent applications using Ni deposition for enhancing the photoreforming activity of organics. For example, Tian et al. [135] observed enhanced performance of Ni/ZrO_2 nanorods for ethanol photothermal dry reforming in a temperature range of 350–550 °C, with samples prepared by precipitation outperforming samples prepared by impregnation thanks to stronger $NiO−ZrO_2$ interaction. Ni acted as the electron sink, capturing photoexcited electrons which were then transferred to CO_2 for reduction to CO, while electron holes migrated to the ZrO_2−Ni interface, were they activated ethanol for reaction with the O^{2-} species produced by the previous reduction of CO_2. Interestingly, the use of Ni and Ce as co−dopants for ZrO_2 appears greatly favorable for the methane dry reforming reaction: Du et al. [136] observed that the addition of a small amount of CeO_2 to a Ni/ZrO_2 photocatalyst led to a dramatic increase in hydrogen and CO yields, going from a 542 mmol/(g·h) H_2 yield and a 534 mmol/(g·h) CO yield for the Ce−free sample to a H_2 yield of 713 mmol/(g·h) and CO yield of 693 mmol/(g·h) for a

catalyst with 5% wt. Ce addition at 700 °C and a 30 suns irradiation intensity for methane reforming. The addition of cerium dioxide provided sites for oxygen vacancy formation and the activation of carbonated intermediates and contributed to reduced coke formation, with light increasing the generation of surface oxygen vacancies and, thus, increasing the number of active adsorption sites while also providing the active electrons. Similarly, Cheng et al. [137] observed high CH_4 and CO_2 conversions of 51.6% and 56.4%, respectively, for methane photothermal dry reforming at 600 °C over Ce−doped Ni−ZrO_2 catalyst, with CO and H_2 yields of mmol/(g·h) and 83.8 mmol/(g·h), respectively. The addtion of Ce led to a drop in band gap energy from 3.08 to 2.04 eV, and, at the same time, a charge redistribution occurred on material surface, leading electrons to migrate from Ce species to O atoms. An internal electric field is formed in the material, which enhances electron redistribution to Ni clusters during light exposure and enhances charge separation. The formation of oxygen vacancies activates CO_2 and enables the avoidance of coke deposition. Tengfei et al. [138] enhanced the performance of Ni/CeO_2−ZrO_2 catalyst by encasing it in a core–shell structure using SiO_2: the resulting catalyst proved stable over 60 h of prolonged reaction, providing CH_4 and CO_2 conversions as high as 63.5% and 55.9%, respectively, with H_2 and CO yields of 137.0 mmol/(g·h) and 182.9 mmol/(g·h), respectively, at 600 °C. Light irradiation considerably lowers the activation energy of the reaction compared to pure thermal process. The addition of nickel–cerium and the core–shell structure were observed to greatly reduce the band gap energy compared to pure ZrO_2. Most recently, Liu et al. [139] conducted a detailed investigation of tailoring of surface properties of a Ni/$CeZrO_2$ photocatalyst through a MOF structure and achieved conversions of CH_4 and CO_2 as high as 63.9% and 71.1%, respectively, at 650 °C, with the catalyst remaining stable for 250 h of continued reaction. The MOF structure showed resistance to carbon deposition and improved charge separation capacity. The reaction mechanism involved the transfer of electrons to Ni clusters and CO_2 activation to carboxylic intermediates, similar to previous studies.

The deposition of nickel nanoparticles combined with La_2O_3 and ZrO_2 was tested by Meng et al. [140], where 10Ni/$La_2Zr_2O_7$ demonstrated the highest catalytic activity, with production rates of H_2 and CO of 4572 mmol/(g·h) and 5946 (g·h), respectively. Ni acted as the methane activation site, while oxygen vacancies on the La_2O_3 surface activated carbon dioxide, with light irradiation improving the stability of the vacancies. Light was also observed to inhibit reverse water–gas shift reaction.

As per nickel−free catalysts, Mendoza et al. [141] synthetized nanorods of Bi_2S_3 supported on ZrO_2 and found them to be effective for the production of hydrogen from methanol in an aqueous solution: the H_2 yield was 4440 μmol/(g·h) for 6% wt. Bi_2S_3/ZrO_2 under UV light, six times the yield for bare ZrO_2, and 1476 μmol/(g·h) under vs. light. The Bi_2S_3 nanorods acted as electron sinks for the photoexcited electrons of ZrO_2. On the other hand, Yu et al. [142] obtained promising performance for a mixed Cu/Zn/Zr oxides catalyst for the reforming of aqueous−phase methanol at temperature as low as 130 °C under 16 suns of irradiation. ZrO_2, ZnO, and CuO oxides are proposed to work as sequential type I heterojunctions, with both electrons and holes migrating to CuO from ZrO_2 using ZnO as a carrier. At the same time, ZnO accepts hydrogen cations produced by the activation of methanol, and the photo−excited electrons accelerate the production of formate intermediate species.

Table 2 summarizes the ZrO_2 catalysts herein discussed.

2.4. C_3N_4−Based Catalysts

Graphitic carbon nitride (C_3N_4)−derived materials are another common choice for photocatalytic reforming applications [143,144]: compared to TiO_2, C_3N_4 possesses a

narrower band gap and is, thus, intrinsically more active under vs. light irradiation, while being metal free and chemically stable; however, it also generally suffers from a more complex preparation, which is an obstacle to scaling up the process, and still requires modification to achieve adequate performance under solar irradiation, particularly to avoid excessive charge recombination [145,146]. Again, noble metals are found to be effective cocatalysts for these applications. Speltini et al. [147] compared the performance of Pt and Cu−Ni cocatalysts supported on either TiO_2 or C_3N_4 for aqueous−phase H_2 production from biomass derivatives and observed overall lower performance for C_3N_4 photocatalysts; it should, however, be noted that C_3N_4 still managed to achieve H_2 yields within 40 to 75% of those obtained on TiO_2. In both cases, the metal cation acted as the hydrogen generation site, while electron holes on the semiconductor surface oxidized the organic substrate. Most recently, Bianchini et al. [148] reported successful pre−pilot scale generation of hydrogen from rice industry wastewater using C_3N_4 with H_2PtCl_6 used as a metal cocatalyst under natural sunlight. They reported an analysis of the process through a response surface model that was used to determine the optimal dilution of the waste to degrade, the optimal catalyst amount, and the optimal loading of the Pt cocatalyst, obtaining their best results with undiluted waste, a 0.5 g/L catalyst concentration, and a 35 wt. Pt loading. Considering the cost of noble metals, the optimization of their load is of great importance in their use as catalysts. While they did not investigate in detail the reaction mechanism, tests of the catalyst in pure water and in dark conditions produced a negligible hydrogen yield, confirming the crucial role that biomass plays as an electron donor and the fundamental role of light in promoting the reaction.

Single−atom metal deposition may offer the possibility for preparing selective catalysts with a low metal load and, thus, reduce cost of noble metal catalyst use: Lazaar et al. [149] deposited highly dispersed Pt atoms on exfoliated C_3N_4, obtaining a maximized H_2 production of 1660 mmol/(g_{Pt}·h) from 10% vol. aqueous triethanolamine solution with a total Pt loading of only 0.03% wt. A dark reactive deposition approach was used to obtain stable single−atom surface species chemically bound to carbon nitride, with Pt atoms being bound to N4 sites with high charge transfer ability. The high dispersion of Pt atoms increased their activity and prevented agglomeration, contributing to catalyst stability and allowing the catalyst to surpass the performance of other catalysts loaded with conventional techniques. The morphology of C_3N_4 also plays an important role in its activity: for example, Pt−loaded ultrathin C_3N_4 nanosheets were found to be more effective than Pt loaded on bulk C_3N_4 for the aqueous reforming of cellulose [150]: the nanosheet structure increased the oxidation potential of the carbon nitride, favoring the formation of hydroxyl radicals that could then react with biomass, while at the same time improving electrical conductivity, reducing band gap, and favoring electron–hole separation. The load of the cocatalyst was essential to optimize the yield, with a 2% wt. load providing optimum performance. On the other hand, the addition of other cocatalysts is also a potentially effective pathway. For example, Gao et al. [151] observed a 3.6−times increase in hydrogen production with a 5% wt. addition of SnS_2, also obtaining an increase in degradation efficiency for methylene blue dye. A type II heterojunction was formed between carbon nitride and SnS_2, with SnS_2 acting as the electron sink. The addition of methyl viologen to the C_3N_4 structure was instead observed to enhance hydrogen production in the aqueous phase with the triethanolamine sacrificial agent [152], with methyl viologen species accumulating electrons formed by the photoexcitation of carbon nitride and accelerating their transfer to Pt cocatalyst, thus inhibiting charge recombination.

Other metal species have been tested as cheaper alternatives to noble metals. Similarly to the previously discussed investigation of Lazaar et al. for single Pt atom deposition, Li et al. [153] maximized the yield of direct methanol synthesis from CH_4 by controlling the

coordination number of single iron atom loading on carbon nitride surface, obtaining a remarkable methanol yield of 928.27 μmol/g for the $Fe_1/C_{3-x}N_4$ with a $Fe-N_3$ coordination. In these conditions, they observed that the reaction proceeded through a three−electron mechanism involving methane adsorption and activation as methyl surface group and the production of hydroxyl radicals from oxygen.

Table 1. TiO_2−based photocatalysts for reforming processes. A = aqueous phase, G = gas phase, AQY = apparent quantum yield, QE = quantum efficiency, and PE = photonic efficiency.

Catalyst	Raw Material	Phase	T (°C)	Product (Max Yield)	Max Light Efficiency (%)	Wavelength	Source
$Pt-Rh_2O_3-TiO_2$ hollow spheres	Methane	G	300	H_2 19.8 mmol/(g·h)	3.51	UV light (Hg−Xe lamp)	[109]
$Pt-TiO_2$	Naphthalene	A	25	–	PE 0.97% H_2 production PE 0.33% naphthalene conversion	Simulated sunlight (Xe lamp)	[110]
$Pt-Nb_2O_5-TiO_2$	Ethanol	A	25 (UV light) 40 (Natural sunlight)	H_2 138 mmol/(g·h) UV light H_2 40 mmol/(g·h) natural sunlight	AQY 44% (UV light) AQY 85% (UV fraction of sunlight).	365 nm Natural sunlight	[111]
NiO−Ni−TiO_2 heterojunction	Glycerol	A	–	H_2 24.5 mmol/(g·h) dihydroxyacetone, glyceraldehyde	–	Simulated sunlight (Xe lamp)	[112]
MOF−derived $(O-Ni_2)/TiO_2$	Glycerol	A	10	H_2 2.5426 mmol/(g·h) CO 0.3617 mmol/(g·h)	–	365 nm	[113].
Ni/mesoporous TiO_2	Methane	G	500–600	H_2 44.85 mmol/(g·h) CO 68.78 mmol/(g·h)	–	Simulated sunlight (Xe lamp)	[114]
$Ni-TiO_2$	Methane	G	–	H_2 87.4 mmol/(g·h) CO 220.2 mmol/(g·h)	–	Simulated sunlight (Xe lamp)	[115]
$CuNi/TiO_2$	Cellulose	A	15	H_2 0.489 mmol/(g·h) CO_2 0.224 mmol/(g·h) Sugars * Anions **	–	365 nm	[116]
Cu_2O-TiO_2	Methanol, ethanol, ethylene glycol, formic acid, glycerol, lactic acid	A	20–80	H_2 250 μmol/L	8	>400 nm Natural sunlight	[117]
Cu_2O-TiO_2 (P25)	Glycerol, glucose, ethanol	A	Max 45	H_2 7.54 mmol/(g·h) Carboxylic acids	1.7	Natural sunlight	[118]
Cu−based MOF/TiO_2	Methanol	A	–	H_2 13.24 mmol/(g·h)	–	Simulated sunlight (Xe lamp)	[119]
Cu_2O/TiO_2, $Cu_2O/TiO_2/Cu$ TiO_2/Cu heterojunctions	Methanol	A	–	H_2 0.27953 mmol/(g·h) CO 0.01058 mmol/(g·h)	–	Simulated sunlight (Xe lamp)	[120]
Cu−TiO_2 (one−pot hydrothermal method)	Cellulose	A	25	H_2 2.752 mmol/(g·h) CO_2 1653 mmol/(g·h) Sugars Organic acids		365 nm	[121]
Mesoporous Cu/TiO_2-CeO_2	Methanol	G	200–300	H_2 78.8 mmol/(g·h)	–	UV light (280–400 nm)	[122]
Co−TiO_2	Glycerol acetonitrile	A	34.85	Formic acid 57% Formaldehyde 21%	–	365 nm	[123]
$Co_xNi_{1-x}Se/TiO_2$	TEOA	A	30	H_2 10.079 mmol/(g·h)	–	Simulated sunlight (Xe lamp)	[124]
La−TiO_2	Methane	G	–	H_2 1.458 mmol/(g·h)	–	UV light (Hg lamp)	[125]
W−TiO_2	Ethylbenzene	A	25	Acetophenone 235 mmol/g	0.7	437 nm	[126]
MoS_2-TiO_2	α−cellulose biomass ***	A	Max 60	H_2 1.653 mmol/(g·h) (cellulose) H_2 0.05 mmol/(g·h) (corncob)	AQY 5.62% 380 nm	Simulated sunlight (Xe lamp)	[127]
Carbon dot−TiO_2	Ethanol	A	–	H_2 0.5436 mmol/(g·h)	–	Simulated sunlight (Xe lamp)	[128]
TiO_2 nanotubes	Cellulose	A	–	CH_4 17.020 mmol/g CO 213,690 mmol/g Glucose	–	Simulated sunlight (Xe lamp)	[129]
Biphasic TiO_2	Methane	A	25	Formaldehyde 24.27 mmol/g	QE 3.28% 313 nm QE 2.52% 365 nm	Simulated sunlight (Xe lamp)	[130]
MOF−derived engineered TiO_2	Methane	G	–	C_2H_6 0.0037 mmol/(g·h)	–	Simulated sunlight (Xe lamp)	[131]
Anatase TiO_2	Toluene	G	–	98% toluene abatement H_2 yield > 60%	–	UV−VS light generated by microwave–metal discharge	[132]

* Arabinose, glucose, xylose, mannose, cellobiose, and maltose; ** acetate, formate, and oxalate; *** rice straw, corn straw, wheat straw, rice husk, soybean straw, and corncob.

Table 2. ZrO_2−based photocatalysts for reforming processes. A = aqueous phase; G = gas phase.

Catalyst	Raw Material	Phase	T (°C)	Product (Max Yield)	Max Light Efficiency (%)	Wavelength	Source
Ni/ZrO_2 rods	Ethanol	G	350–550	Max ethanol conversion = 70% H_2 and CO selectivity > 40%	–	Simulated sunlight (Xe lamp)	[135]
Ni−CeO_2−ZrO_2	Methane	G	700	H_2 713 mmol/(g·h) CO 693 mmol/(g·h)	–	Simulated sunlight	[136]
Ni−Ce−ZrO_2	Methane	G	400–600	H_2 83.8 mmol/(g·h) CO 59.1 mmol/(g·h)	–	Simulated sunlight (Xe lamp)	[137]
Ni/CeO_2–ZrO_2@SiO_2 core–shell structure	Methane	G	400–600	H_2 137.0 mmol/(g·h) CO 182.9 mmol/(g·h)	–	Simulated sunlight (Xe lamp)	[138]
MOF−derived Ni/$CeZrO_2$	Methane	G	400–650	H_2 171.7 mmol/(g·h) CO 182.6 mmol/(g·h)	–	Simulated sunlight (Xe lamp)	[139]
Ni/$La_2Zr_2O_7$	Methane	G	700	H_2 4572 mmol/(g·h) CO 5946 mmol/(g·h)	–	Simulated sunlight (Xe lamp)	[140]
Bi_2S_3 nanorods/ZrO_2	Methanol	A	–	H_2 4.440 mmol/(g·h) in UV light H_2 1.476 mmol/(g·h) in vs. light		254 nm UV light (high pressure Hg lamp pen−ray) 540 nm vs. light (blue LED lamps)	[141]
Cu/Zn/Zr oxide nanocatalysts	Methanol	G	130	H_2 67.37 mmol/(g·h)	45.6% solar–chemical conversion efficiency	Simulated sunlight (Xe lamp)	[142]

Hierarchical carbon nitride structure (H−C_3N_4) also demonstrated enhanced and stable activity for methane dry and bi−reforming, as well as methanol reforming [154], which was further enhanced by cobalt doping: under dry methane reforming with stoichiometric feed, an optimized 2% wt. Co/H−C_3N_4 achieved CO and H_2 evolution rates of 555 and 41.2 µmol/(g·h), respectively, an increase of 18.28− and 1.74−fold than when using H−C_3N_4, itself possessing 1.85− and 1.81−fold higher yields than graphitic C_3N_4. The higher yields can be attributed to higher charge carrier separation induced by doping and structural modification. For photocatalytic bi−reforming of methane, the production of CO and H_2 was reduced, whereas significantly higher CO and H_2 evolved using the bi−reforming of methanol, achieving 10.77− and 1.39−fold more H_2 and CO efficiency compared to dry reforming of methane in the latter case. In both cases, cobalt acted as the electron sink enhancing charge separation, while organizing the carbon nitride into layered hierarchical structure improved its own charge separation capacity by forming defects. CO and H_2 were the main reaction products, produced from the transfer of two electrons.

The formation of heterojunctions of carbon nitride with other semiconductors was investigated by other authors. Khan et al. [155], for example, investigated the use of cobalt aluminum lanthanum−layered double hydroxide (LDH) as a support for a TiO_2−Ti_3C_2 and C_3N_4 mixture in methane bi−reforming with water and carbon dioxide. The strong interaction between the three species allowed the researchers to reduce the charge carrier recombination, and the material reached maximum production of 24.35 µmol of production for CO at a catalyst loading of 0.13 g with a feed ratio of 1.67 at 4.47 h, while the maximum H_2 production of 21.91 µmol was achieved at a catalyst loading of 0.14 g with the feed ratio of 1.41 at 4.93 h. A four−step heterojunction was formed between Ti_3C_2, TiO_2, C_3N_4, and the cobalt−based LDH, with electrons concentrated on the carbide and LDH species. S−scheme heterojunctions formed between TiO_2 and LDH and between TiO_2 and carbon nitride, allowing for efficient charge transfer and separation. The good integration of all the catalyst species also allowed the enhancement of the surface area, thus favoring reactant adsorption. Tahir et al. observed an enhancement in reforming performance by addition of 15% wt. $La_xCo_yO_3$ perovskite for aqueous phase reforming of methanol [156], also forming an S−scheme heterojunction. Similarly promising results were also observed for S−scheme heterojunction composites prepared by the combination of C_3N_4 with $MnMgPO_4$ [157]. S−scheme C_3N_4 heterojunctions have also received interest for the photodegradation of plastic waste, with Mohanty et al. [158] observing a

hydrogen evolution rate of 12.6 ± 2 mmol/(g·h) for combined $C_3N_4/\alpha-MnO_2$ with the concurrent formation of value−added organic molecules (benzaldehyde, benzoic acid, toluene, benzene, and carbonic acid) from polystyrene reforming.

A metal−free modification of carbon nitride was instead attempted by Ikreedeegh and Tahir [159], who deposited graphene oxide (GO) nanosheets on a carbon nitride surface by a sonochemical thermal−assisted method and then tested the material for methane dry reforming under vs. light: they observed that a 0.5% wt. addition of graphene oxide increased the yield of CO up to 5 times compared to unmodified material, while a 0.25% wt. addition maximized H_2 production. They also observed that dry reforming carried out with a stoichiometric CO_2/CH_4 ratio (1:1) performed better than both steam and bi−reforming on this catalyst; however, the quantum yields of the catalysts were still below 0.4% even for the optimized graphene oxide loading. The activity of the material in this case was enhanced by the graphene oxide acting as electron sink, similarly to what is commonly obtained through the loading of metal species. On the other hand, Xie et al. [160] demonstrated that carbon ring inclusion in C_3N_4 can potentially provide a pathway for photocatalyst activation under low−energy near−infrared light (NIR) for the degradation of lignocellulosic material coupled with H_2 production. The inclusion of carbon graphitic rings in the catalyst structure introduced intermediate energy levels in the band gap structure, allowing the adsorption of near−infrared radiation, and created regions of low electron density, polarizing the surface and facilitating electron migration and charge separation.

Table 3 summarizes the literature reviewed for C_3N_4−based photocatalysts.

2.5. Other Catalysts

While the previously discussed TiO_2, ZrO_2, and C_3N_4 remain the most investigated materials for photocatalytic reforming processes, a number of other materials have also been tested as possible alternatives. Perovskite−based photocatalysts, for example, have been tested by Chung et al. [161] in an innovative combined plasma–photocatalytic process for methane dry reforming: synergistic effects between plasma− and photocatalysis contributed to increasing the H_2 yield, and among $LaFeO_3$, $NiTiO_3$, and $AgNbO_3$, the former displayed the highest performance in terms of both reactant conversion and energy efficiency. Not only are methane and CO_2 pre−excited by exposure to the high electron temperature plasma, but the photocatalyst can be excited by plasma−produced photons, as well as by the capture of previously emitted free electrons. Plasma exposure can modify the photocatalyst surface structure and reduce particle aggregation, and the presence of a photocatalyst may enhance the power of plasma discharge thanks to photocatalyst polarization. In their further work [162], they concluded that $LaFeO_3$ calcined at 600 °C demonstrates optimized CH_4 and CO_2 conversions and syngas generation efficiency of 53.6%, 40.0%, and 18.4 mol/kWh, respectively. On the other hand, $LaFeO_3$ doped with 0.12% wt. Ni was observed to be active also for photoreforming of glucose to hydrogen in aqueous solution, with H_2 yield of 2574 µmol/L after 4 h of UV irradiation [163]. Hydrogen was primarily produced from water reduction over Ni atom electron sinks, while glucose played the role of the hole scavenger. Hydroxyl radicals were identified as the main reactive species involved in the oxidative degradation process. Another perovskite, $LaMn_xNi_{1-x}O_3$ ($0 \leq x \leq 1$), proved effective for the coupled thermo−photocatalytic conversion of toluene as a tar model compound [164], with 90% carbon conversion of toluene obtained on $LaMn_{0.4}Ni_{0.6}O_3$ at 400 °C. The formation of oxygen vacancies and activated oxygen species under material irradiation was observed to play an important role in the adsorption and conversion of toluene. Overall, temperature and light displayed a synergistic effect on pollutant degradation.

Table 3. C_3N_4−based photocatalysts for reforming processes. A = aqueous phase, G = gas phase, AQY = apparent quantum yield, APE = apparent photon efficiency, GO = graphene oxide, LDH = layered double hydroxide, and NIR = near−infrared.

Catalyst	Raw Material	Phase	T (°C)	Product (Max Yield)	Max Light Efficiency (%)	Wavelength	Source
Pt−oxidized g−C_3N_4	Glucose	A	–	H_2 1.370 mmol/(g·h)	AQY 0.8% (native pH) AQY 1.3% (pH 11).	Simulated sunlight, natural sunlight	[147]
Pt−Poly(heptazine imide)−C_3N_4	Glucose, rice milk wastewater	A	–	H_2 1.000 mmol/(g·h) (glucose) H_2 0.150 mmol/(g·h) (rice milk wastewater) H_2 0.11P5 mmol/(g·h) (rice milk wastewater, natural sunlight)	–	Simulated sunlight, natural sunlight	[148]
Single−atom Pt−C_3N_4	TEOA	A	–	H_2 1660 mmol/(g_{Pt}·h)	–	LED 365 nm	[149]
Pt−2D C_3N_4 nanosheet	Cellulose	A	–	H_2 0.09433 mmol/(g·h) in NaOH 3M		Xe lamp with a UV cut−off filter (400 nm < λ < 780 nm)	[150]
Pt−SnS_2/C_3N_5	TEOA	A	60	H_2 0.9225 mmol/(g·h)	–	Xe lamp with a vs. light cut−off filter (λ: 400−780 nm)	[151]
Pt−methyl viologen−C_3N_4	TEOA	A	–	H_2 1.65 mmol/(g·h)	–	Xe lamp with a UV cut−off filter (λ > 420 nm)	[152]
Fe−C_3N_4	Methane	A	25	Methanol 0.92827 mmol/g	–	Simulated sunlight (Xe lamp)	[153]
Co−C_3N_4	Methane, methanol	G		Methane dry reforming: CO 0.555 mmol/(g·h) H_2 0.0412 mmol/(g·h) Methanol bi−reforming: CO 0.771 mmol/(g·h) H_2 0.444 mmol/(g·h)	–	Hg lamp	[154]
g−C_3N_4/$TiO_{2A/R}$@Ti_3C_2/CoAlLa−LDH	Methane	G	27	H_2 0.04150 mmol/(g·h) CO 0.03734 mmol/(g·h)	AQY 0.407% CO AQY 0.363% H_2	Xe lamp 420 nm	[155]
$La_xCo_yO_3$−3D g−C_3N_4 hollow tube	Methanol	A	25	H_2 0.070 mmol/(g·h)	APE 0.58%	Xe lamp λ ≥ 420 nm	[156]
$MnMgPO_3$−C_3N_4	Methylene blue, oxytetracycline, tetracycline	A	25	H_2 3.595 mmol/(g·h)	–	VS light (Xe lamp)	[157]
α−MnO_2/g−C_3N_4	Polystyrene	A	–	H_2 12.6 mmol/(g·h) benzaldehyde, benzoic acid, toluene, benzene, and carbonic acid	–	Xe lamp	[158]
GO−g−C_3N_4	Methane	G	–	H_2 0.03024 mmol/(g·h) (0.25% wt. GO) CO 0.3991 mmol/(g·h) (0.5% wt. GO)	AQY 0.9% (0.5% wt. GO)	Simulated sunlight (Xe lamp)	[159]
g−C_3N_4−C_x carbon ring Modified C_3N_4	α−cellulose Lignocellulose	A	25	H_2 2.1 μmol/h (NIR irradiation) mannose, galacturonic acid, glucuronic acid, galactose, lactic acid, formic acid, and 5−hydroxymethyl furfural	AQE 4.7% at 550 nm	Xe arc lamp coupled with a λ ≥ 630 and λ ≥ 800 nm filter	[160]

Cerium dioxide also found interest in its use as a primary photocatalyst rather than only as an additive: Tavasoli et al. [165] investigated the use of Ni−supported catalysts on selectively phosphated CeO_2 nanorods for the hybrid photothermal dry reforming of methane, obtaining results close to the ones obtained for noble metal catalysts. The phosphate groups allowed the researchers to tune the ceria surface alkalinity, and again temperature and light adsorption were observed to synergistically contribute to conversion. Light exposure enhances formation and promotes the reaction of surface carbonyl species, The combined catalyst proved to be active even under visible light−only monochromatic irradiation. Balsamo et al. [166] coupled cerium dioxide and graphene oxide to the use of an Au cocatalyst and obtained a 270 μmol/(g·h) H_2 evolution rate from aqueous−phase 10% vol. glycerol solution under simulated sunlight. The material displayed stable operation, and hydrogen yield increased following the reduction of graphene oxide after five operation cycles. The graphene oxide acted as a mediator for the transfer of electrons from cerium to gold atoms. Iannaco et al. [167] performed photocatalytic hydrogen generation

from lactic acid rich solutions, obtaining a hydrogen production of 3989 μmol/L for sample prepared with the supercritical antisolvent technique, higher than those obtained for commercial CeO_2 powder (2519 μmol/L). The addition of an optimal CuO amount of 0.5% wt., determined an increase in hydrogen production of up to 9313 μmol/L after 4 h of UV irradiation time. They also confirmed that water acted as the hydrogen source, while lactic acid acted as sacrificial agent to refill the electron holes of the catalyst. The ceria and CuO interaction formed a type I heterojunctions, with electrons and holes being transferred to CuO. Zhang et al. [168] observed that the surface dispersion of Cu atoms over the CeO_2 surface affected greatly the degradation of aqueous−phase toluene, with more even distribution of active sites $Cu^+-Ov-Ce^{3+}$ improving the adsorption and activation of reactants. On the other hand, surface lattice oxygen accelerates the rate−determining step of benzoate deep decomposition. The toluene degradation pathway was toluene → benzyl alcohol → benzaldehyde → benzoate →anhydride → CO_2 and H_2O. Aoun et al. [169] observed that a 15% wt. $SrNiO_3-CeO_2$ composite rapidly oxidated 2−propanol under both UV−LED and vs. light. A type I heterojunction was formed between ceria and the perovskite, with electrons and holes migrating to $SrNiO_3$. Li et al. [170] synthetized a S−scheme heterojunction by depositing $AgInS_2$ quantum dots on CeO_2 surface and obtained the selective oxidation of xylose to xylonic acid and CO under vs. light (xylonic acid yield = 60.0%, CO evolution rate = 3689.9 μmol/(g·h)). On the other hand, Wang et al. [171] prepared a noble metal−free CeO_2/CdS/NiS triple heterojunction with remarkable photocatalytic performance for the degradation of plastic waste, obtaining a hydrogen production rate of 32.40 mmol/(g·h) at the fifth hour, 29 times that of bare CdS and 463 times that of bare CeO_2. In this case, Ni S was proposed to act as electron mediator between CdS and ceria conduction bands, with ceria acting as hydrogen production site and CdS electron holes carrying out the oxidation of waste.

WO_3 is another material that has been tested for photocatalysis. Li et al. [172] reported the synthesis of a 2D CoP S−scheme heterojunction over a 0−dimensional WO_3 support for H_2 generation from a triethanolamine aqueous solution. CoP acted as the electron sink, while WO_3 accumulated the electron holes. They obtained 218.63 mmol of hydrogen under vs. light exposure within 5 h of reaction, 287 times the amount of hydrogen formed for pure WO_3 and 1.95 multiples the one produced from pure CoP. Similarly, the addition of CuO to WO_3 increased the hydrogen yield from aqueous methanol solution by 64 times [173]. Surface oxygen vacancies capture the oxygen atom of CH_3OH, while the Cu^{2+} cations activate the C−H bond. During the process, CH_3OH accepts photogenerated electrons from WO_3 and provides electrons to Cu^{2+}. The addition of WO_3 and graphene to TiO_2 increased the catalytic activity for gaseous phase benzene degradation and hydrogen production [174]: the addition of WO_3 only forms a type II heterojunction, improving charge separation, but reduces the activity compared to pure TiO_2 due to the low potential of the photoexcited electrons. On the other hand, the addition of graphene not only facilitates electron transfer, but also offers a surface with a potential more suitable for hydrogen generation, thus compensating activity loss. However, despite the higher hydrogen production, the graphene−modified catalysts still display low oxidation capacity towards benzene. N−n heterojunction $CuMn_2O_4/WO_3$ nanocomposites constructed by a sol–gel procedure were evaluated for H_2 evolution from aqueous glycerol under vs. light by Albukhari et al. [175]. Their optimized 12% wt. $CuMn_2O_4/WO_3$ nanocomposite exhibited a high maximal H_2 evolution rate of 2856.6 μmol/(g·h). An S−scheme heterojunction transfers electrons from WO_3 to $CuMn_2O_4$, which are then concentrated on Pt species.

Other catalytic systems were also investigated. Ye et al. [176], for example, investigated the use of 2D $V_xW_{1-x}N_{1.5}$ bimetallic systems as cocatalysts coupled with CdS for the reforming of formic acid to syngas. A formulation of $V_{0.1}W_{0.9}N_{1.5}$ boosted performance by over

60% compared to the unmodified W_2N_3 system. The $V_xW_{1-x}N_{1.5}$ species acted as electron sinks for electrons of CdS. Zhou et al. [177] used Ni nanoparticles loaded on mesoporous silica for the photo−thermocatalytic steam reforming of cellulose under UV−VS light and obtained high production rates of H_2 and CO (1966.2 and 1257.7 mmol/(g·h)) together with a light−to−fuel efficiency of 5.5%. On the other hand, Zhong et al. [178] performed the same reaction while using Ni nanoparticles loaded on θ−Al_2O_3, and they obtained significantly higher production rates of syngas (H_2 3776.3 and CO 2028.1 mmol/(g·h)) and no deactivation after four cycles. In both cases, light and heat acted synergically to enhance reaction rate, and the degradation of cellulose followed a pyrolytic mechanism.

The literature on the catalysts discussed is summarized in Table 4.

Table 4. Other photocatalysts for reforming processes. A = aqueous phase, G = gas phase, L = liquid phase, and AQY = apparent quantum yield.

Catalyst	Raw Material	Phase	T (°C)	Product (Max Yield)	Max Light Efficiency (%)	Wavelength	Source
$NiTiO_3$, $LaFeO_3$ $AgNbO_3$	Methane	G	650–680	$LaFeO_3$ calcined at 600 °C: CH_4 conversion 61.9% CO_2 conversion 61.9% H_2 selectivity 82.5% CO selectivity 69.9%	–	Light from plasma generation system, simulated sunlight (Xe lamp)	[161]
$LaFeO_3$	Methane	G	650–680	CH_4 conversion 53.5% CO_2 conversion 40.0% H_2 selectivity 85.0% Co selectivity 71.8%	–	Light from plasma generation system	[162]
Ni−$LaFeO_3$	Glucose	A	–	H_2 2.573 mmol/L	–	UV lamps (emission peak at 365 nm)	[163]
$LaMn_xNi_{1-x}O_3$	Toluene	G	400	90% toluene conversion	–	Xe lamps λ = 350–780 nm	[164]
Phosphated Ni−CeO_2 nanorod	Methane	G	350	Stable H_2 and CO rate ≈ 5 mmol/(g·h) at 48 suns for sample with P/Ce = 0.65	–	UV light, red light, blue light, green light	[165]
Au−CeO_2−rGO	Glycerol	A	–	H_2 0.270 mmol/(g·h)	–	Simulated sunlight (Xe lamp)	[166]
CuO−CeO_2	Lactic acid	A	450	H_2 ≈ 2.6 mmol/(g·h)	AQY 0.459%	UV light 365 nm	[167]
Cu−CeO_2	Toluene	A	200–231	Toluene conversion 89.9%	–	Simulated sunlight (Xe lamp)	[168]
$SrNiO_3/CeO_2$	2−propanol	G	–	100% propanol conversion	–	UV lamp 365 nm Xe lamp 315–400 nm	[169]
$AgInS_2$ quantum dots−CeO_2	Xylose	A	30–80	Xylonic acid yield 60.0% CO 3.6899 mmol/(g·h) H_2 32.40 mmol/(g·h)	–	VS light	[170]
CeO_2/CdS/NiS	Polylactic acid hydrolysate	A	6	pyruvate, acetate, and formate	–	VS light (Xe lamp)	[171]
2D CoP supported 0D WO_3	TEOA	A	–	H_2 0.21863 mmol in 5 h	AQY 2.02% 520 nm	VS light 450, 475, 500, 520 and 550 nm	[172]
CuO/WO_3	Methanol	L	25	H_2 0.0996 mmol/(g·h)	–	VS light	[173]
TiO_2/WO_3/graphene	Benzene Methanol	A	–	H_2 0.054 mmol/g in 4 h from methanol	–	Simulated sunlight	[174]
Pt−$CuMn_2O_4/WO_3$	Glycerol	A	–	H_2 3.472 mmol/(g·h)	–	Xe lamp λ > 420 nm	[175]
2D $V_xW_{1-x}N_{1.5}$ + CdS	Formic acid	A	25	H_2 0.18404 μmol/h	–	Simulated sunlight (Xe lamp)	[176]
Ni−SiO_2	Cellulose, rice straw, wheat straw, corn stalk, kitchen waste		500–700	Cellulose: H_2 1966.2 mmol/(g·h) CO 1257.7 mmol/(g·h) Rice straw: H_2 1488.1 mmol/(g·h) Wheat straw: H_2 728.4 mmol/(g·h) Corn stalk: H_2 1036.5 mmol/(g·h) Kitchen waste: H_2 760.4 mmol/(g·h)	Light−to−fuel efficiency 5.5% (cellulose)	Xe lamp	[177]
Ni/θ−Al_2O_3,	Cellulose	A	200–700	H_2 3776.3 mmol/(g·h) CO 2028.1 mmol/(g·h)	–	λ > 420 nm, and λ > 560 nm	[178]

3. Reactor and Process Design

Like photovoltaic generation, the requisite for the utilization of a photocatalyst in chemical reactors is the availability of a suitable light source and low attenuation of the irradiated power. Packed bed reactors, filled in with monoliths or granules, that are normally used for catalytic reactions even at high superficial velocity [179], are not usable because of the large attenuation of the irradiation in the bulk.

Conversely, a typical photoreactor has a planar or two−dimensional geometry, like in the "carpet", "pancake", "toothpick", and "honeycomb" schemes reported in Figure 4 [180], with a transversal or longitudinal irradiation. The photocatalyst powder is dispersed and fixed over a suitable support that can be easily irradiated by natural or artificial light. The reactant is in contact with the catalyst mainly by a rather laminar flow, resulting in poor process intensification. Apart from reactions occurring in liquids, this configuration is suitable for the removal of pollutants from the environment, e.g., indoor air purification [181]. Photocatalytic CO_2 reduction by steam has recently been addressed at laboratory−scale or modelled, demonstrating the possibility of distributed H_2 production, even with solar irradiation [182,183].

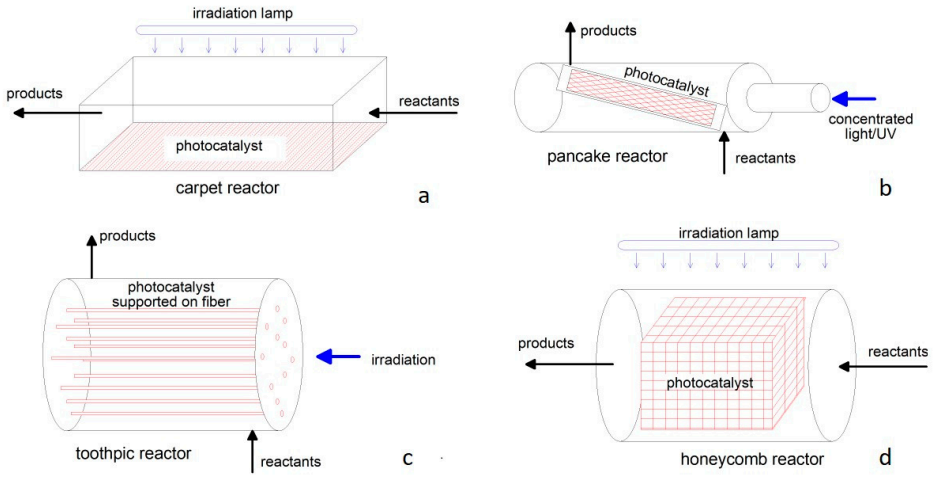

Figure 4. Configurations of planar or two−dimensional photoreactors: (**a**) carpet; (**b**) pancake; (**c**) toothpick; (**d**) honeycomb.

Fluidized bed (FB) technology has been largely adopted for catalytic heterogeneous reactions thanks to its good mixing, excellent heat and mass transfer, and process reliability [184]. Normally, the FB reactor operates with a dense phase that is fluidized by a gas stream at velocities higher than the minimum for fluidization (U_{mf}). Diluted fluidized beds are operated at a high gas velocity equal or higher than the terminal velocity U_t of the particle, thus allowing large plant potentiality. Therefore, FBs perform well when large diffusion coefficients and high heat transfer are needed for the catalytic process, for instance in the case of steam [185] and dry [186] reforming of hydrocarbons. They also allow easy regeneration of spent catalysts by looping with an external unit operated at different temperatures and atmosphere [187]. Nowadays, the utilization of photocatalytic fluidized beds is limited to only a few research activities dealing with pollutant conversion [188]. The photocatalytic elimination of phenol−derived compounds was studied in an FB reactor with a liquid/solid emulsion provided with a concentric UV light source [189]. The process efficiency increased with decreasing particle size, even for the same surface area concentration, with larger particles causing a blocking effect between the light source and the catalyst surface. Similarly, an excess of particle holdup caused light shielding, and an optimum bed concentration of 20 g/L of mixture was determined. Photocatalytic degradation of aromatics was successfully investigated in a FB photoreactor at lab−scale equipped with a UV source, taking advantage of the increased mass transfer [190]. For a non−purification−related application, Vaiano et al. [191] addressed the photocatalytic reduction of CO_2 in FB via a steam reaction. They reported that an optimized formulation of the photocatalyst based on Ti and Pd, along with a UV−illuminated fluidized bed, can effectively allow the photocatalytic conversion of CO_2, under mild reaction conditions.

The utilization of fine photocatalytic particles that are typically used over supports in other devices, e.g., self−cleaning TiO_2 coating [192], is problematic in fluidized beds due to channeling and poor fluidization according to the Geldart classification of particulates [193]. In this respect, the synergy with other physical phenomena, like magnetism or sound [194,195], may significantly improve the quality of fluidization and the whole performance of the photocatalytic reactor. More frequently, the active phase is deposited over easily fluidizable and mechanically resistant particles, for instance γ−alumina, as reported for tar abetment in a FB gasifier [196]. In the case of photocatalytic reactions, the internal surface area could result inaccessible to irradiation, but inner sites may be suitable for combined steps, e.g., adsorption/release of CO_2, in the whole process [197]. The use of two−dimensional or toroidal geometry systems favors uniform illumination of the catalyst but limits the potential of the system due to the smaller cross−section. Other FB configurations, e.g., conical geometry with an internal jet [198], could be particularly effective in gas–solid mixing and generation of diluted regions for vs. or UV irradiation. Figure 5 displays the different FB configurations.

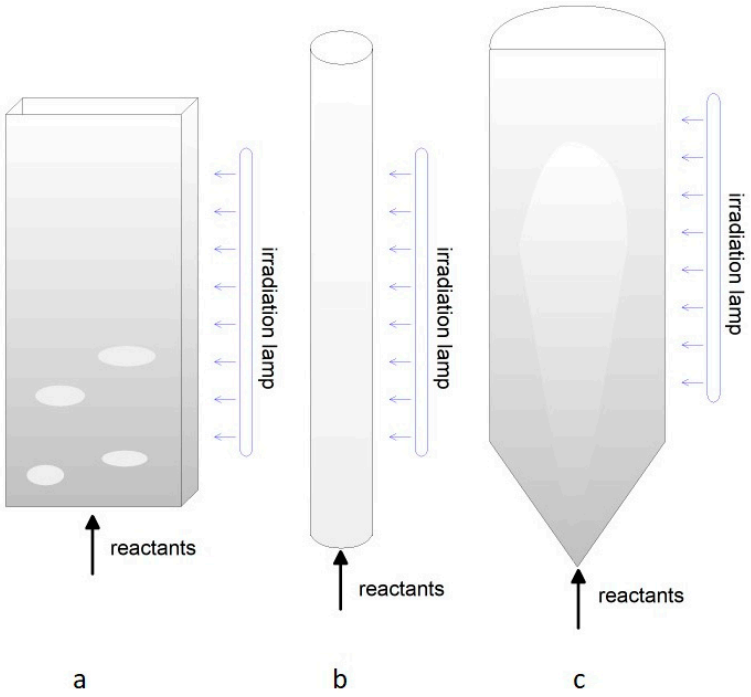

Figure 5. Different designs of fluidized beds: (**a**) dense two−dimensional; (**b**) diluted; (**c**) conical with jet.

In a pioneering work [199], light transmission in a dense 2D fluidized bed was measured and correlated in regimes with up to 10 times U_{mf} showing a rapid attenuation of the flux after a few centimeters. Thus, dense fluidized bed photoreactors can be limited to small−scale applications, as in the case of bidimensional devices, while large reaction chambers can effectively operate with a disperse particle phase [200] and a gas velocity approaching or exceeding U_t. In such transport regime conditions, the solid volume fraction can be limited to about 1%, despite having high solid flows, e.g., 20 kg m^{-2} s^{-1} [201].

Table 5 reports a short comparison between bidimensional and fluidized bed photocatalytic reactors. The 2D fixed configuration is more suitable for carrying out unitary operations, like purification, in easier, scalable, and less demanding equipment. In contrast, combined/intensified processes, requiring mass and heat transfer, are better conducted in FB configuration. The photocatalyst is more easily prepared in the form of fluidizable

granules, for example by spray drying [202], rather than demanding two−dimensional devices, e.g., honeycomb or toothpick devices [180].

Table 5. Comparison between different photoreactor configurations.

	Two−Dimensional	Fluidized Bed
Ease of construction	High	Low
Catalytic device complexity	High	Moderate
Pressure drop	Low	Moderate
Scalability	High	Moderate
Heat removal/supply	Moderate	High
Mass transfer	Moderate	High
Process integration	Low	High
Process intensification	Low	High

Large scale plants for steam or dry reforming may convert up to 300,000 Nm^3/h of methane [203] in multiple channels catalytic reactors, for instance the "Steam reformer tube assembly and method of assembling or retrofitting same" [204]. Since the gas velocity in the packed bed is limited to a few cm/s because of the increased pressure drop at higher velocities, the transversal size of large−scale plants likely exceeds 10 m with a height of 2–3 m [203]. In comparison, the possibility to operate at a higher gas velocity, up to 1 m/s, in fluidized bed reactors [193], may largely reduce the volume of the catalytic reactor. In the case of photocatalysis, the need to provide effective irradiation calls for diluted FB systems (Figure 5b,c) or an array of two−dimensional fluidized beds (Figure 6). Thanks to the great flexibility of FB technology, the development of small−scale integrated systems, e.g., biomass gasification and photoreforming of the generated hydrocarbons, could enable distributed H_2 production, with greater environmental sustainability [205].

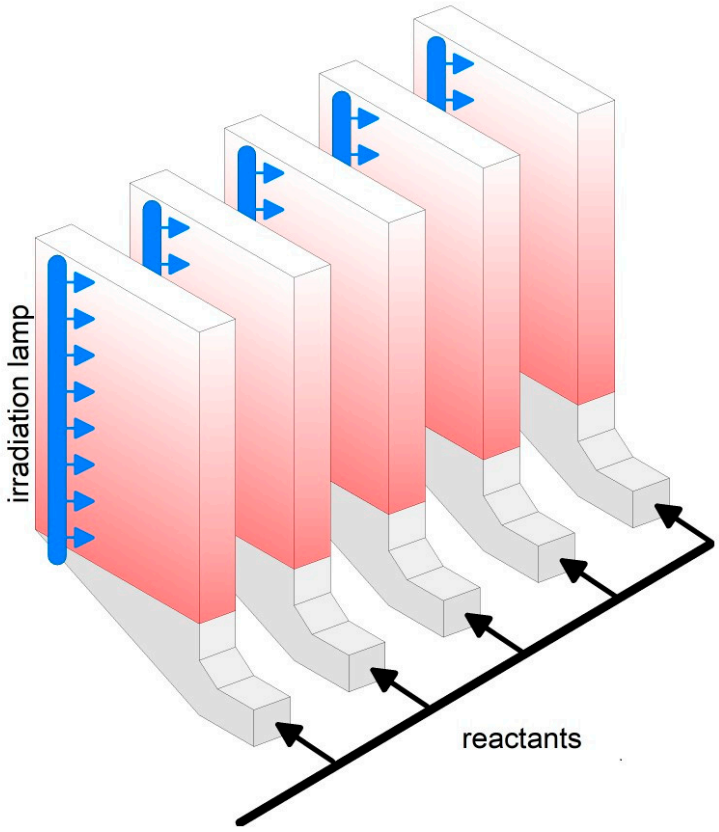

Figure 6. Array of two−dimensional fluidized beds.

The development of the integrated process could benefit from the application of artificial intelligence (AI) and machine learning, both in the development of photocatalytic materials [206] and the optimization of the whole process [207], speeding up the technological progress thanks to increasingly precise predictive models.

4. Conclusions

Titanium oxide is the most diffused material used for photocatalytic processes due to its high activity, good thermal and chemical stability, low cost, and non−toxicity. In the last decades, a lot of research has been carried out to enhance the performance of TiO_2 and to adapt it to different irradiation sources by doping it with other elements or producing nanostructured photocatalysts.

ZrO_2−based photocatalysts possess similar properties as TiO_2, in terms of low cost, high thermal and chemical stability, and mechanical resistance. They can be used under UV light and need modification to operate under VS radiation. Graphitic carbon nitride (C_3N_4) is non−oxidic material suitable for photocatalytic reforming applications, characterized by a narrower band gap and, thus, is intrinsically more active under vs. light irradiation. Conversely, it suffers from a more complex preparation method and related costs.

Overall, prior research has already developed photocatalysts with formulations based on a few elements that are relatively cheap, which allow the development of hydrocarbon reforming processes supported by VS− or UV light.

The application of photocatalysis in large−scale plants and the integration of more processes can be conceived with equipment from the process industry that has so far been scarcely applied in this sector, in particular through the use of fluidization technology. Although these devices may give rise to light attenuation, their superior performance in terms of mixing and energy transport can make up for the limitations of traditional photocatalysis technologies.

With reference to hydrocarbon reforming, the combination of photocatalytic devices and mature plant technologies, such as fluidization, can allow new strategies to obtain better performance and greater flexibility and efficiency, especially in relation to the lower temperature required for the process. Such integration could allow the development of more sustainable processes on a small scale, for example for the photoreforming of biomethane and bio−derivatives obtained from agro−industrial sector.

Although the proposed process integration is still at a low level of readiness, the development of research also supported by powerful artificial intelligence and machine learning tools could allow researchers to achieve pre−industrial solutions in less than 10 years and, therefore, pave the way to commercialization.

Funding: This research was funded by the National Recovery and Resilience Plan (NRRP Italy), Mission 04 Component 2 Investment 1.5—NextGenerationEU, Call for tender no. 3277, dated 30 December 2021.

Conflicts of Interest: The authors declare no conflicts of interest.

Abbreviations

The following abbreviations are used in this manuscript:

A	Aqueous phase
AI	Artificial intelligence
APE	Apparent photon efficiency
AQY	Apparent quantum yield
BG	Band gap
CB	Conduction band

COF	Covalent organic framework
FB	Fluidized bed
G	Gas phase
GO	Graphene oxide
IR	Infrared
MOF	Metal–organic framework
NIR	Near−infrared
L	Liquid phase
LDH	Layered double hydroxide
LED	Light−emission diode
PE	Photonic efficiency
QE	Quantum efficiency
TEOA	Triethanolamine
U_{mf}	Minimum fluidization velocity
U_t	Terminal velocity
UV	Ultraviolet
VB	Valence band
VS	Visible

References

1. Boscherini, M.; Storione, A.; Minelli, M.; Miccio, F.; Doghieri, F. New Perspectives on Catalytic Hydrogen Production by the Reforming, Partial Oxidation and Decomposition of Methane and Biogas. *Energies* **2023**, *16*, 6375. [CrossRef]
2. Großmann, K.; Treiber, P.; Karl, J. Steam Methane Reforming at Low S/C Ratios for Power−to−Gas Applications. *Int. J. Hydrogen Energy* **2016**, *41*, 17784–17792. [CrossRef]
3. Meloni, E.; Martino, M.; Palma, V. A Short Review on Ni Based Catalysts and Related Engineering Issues for Methane Steam Reforming. *Catalysts* **2020**, *10*, 352. [CrossRef]
4. Zhang, H.; Sun, Z.; Hu, Y.H. Steam Reforming of Methane: Current States of Catalyst Design and Process Upgrading. *Renew. Sust. Energy Rev.* **2021**, *149*, 111330. [CrossRef]
5. Wang, S.; Nabavi, S.A.; Clough, P.T. A Review on Bi/Polymetallic Catalysts for Steam Methane Reforming. *Int. J. Hydrogen Energy* **2023**, *48*, 15879–15893. [CrossRef]
6. Lu, H.; Shi, X.; Costa, M.; Huang, C. Carcinogenic Effect of Nickel Compounds. *Mol. Cell. Biochem.* **2005**, *279*, 45–67. [CrossRef] [PubMed]
7. Zhao, X.; Joseph, B.; Kuhn, J.; Ozcan, S. Biogas Reforming to Syngas: A Review. *iScience* **2020**, *23*, 101082. [CrossRef]
8. Jung, S.; Lee, J.; Moon, D.H.; Kim, K.H.; Kwon, E.E. Upgrading Biogas into Syngas through Dry Reforming. *Renew. Sustain. Energy Rev.* **2021**, *143*, 110949. [CrossRef]
9. Minh, D.P.; Siang, T.J.; Vo, D.V.N.; Phan, T.S.; Ridart, C.; Nzihou, A.; Grouset, D. Hydrogen Production from Biogas Reforming: An Overview of Steam Reforming, Dry Reforming, Dual Reforming, and Tri−Reforming of Methane. In *Hydrogen Supply Chain: Design, Deployment and Operation*; Elsevier: Amsterdam, The Netherlands, 2018; pp. 111–166. ISBN 9780128111970.
10. Aramouni, N.A.K. Carbon Mitigation in the Dry Reforming of Methane. Ph.D. Thesis, University of Limerick, Limerick, Ireland, 2020.
11. De Caprariis, B.; Bassano, C.; Deiana, P.; Palma, V.; Petrullo, A.; Scarsella, M.; De Filippis, P. Carbon Dioxide Reforming of Tar during Biomass Gasification. *Chem. Eng. Trans.* **2014**, *37*, 97–102. [CrossRef]
12. Guan, G.; Kaewpanha, M.; Hao, X.; Abudula, A. Catalytic Steam Reforming of Biomass Tar: Prospects and Challenges. *Renew. Sustain. Energy Rev.* **2016**, *58*, 450–461. [CrossRef]
13. Abdelaal, A.; Villot, A.; Patuzzi, F.; Baratieri, M.; Gerente, C. Steam Reforming of Main Tar Compounds over Industrial Gasification Char. *Fuel* **2025**, *384*, 133986. [CrossRef]
14. Sutthiumporn, K.; Maneerung, T.; Kathiraser, Y.; Kawi, S. CO_2 Dry-Reforming of Methane over $La_{0·8}Sr_{0·2}Ni_{0·8}M_{0·2}O_3$ Perovskite (M = Bi, Co, Cr, Cu, Fe): Roles of Lattice Oxygen on C-H Activation and Carbon Suppression. *Int. J. Hydrogen Energy* **2012**, *37*, 11195–11207. [CrossRef]
15. Muraza, O.; Galadima, A. A Review on Coke Management during Dry Reforming of Methane. *Int. J. Energy Res.* **2015**, *39*, 1196–1216. [CrossRef]
16. Aramouni, N.A.K.; Touma, J.G.; Tarboush, B.A.; Zeaiter, J.; Ahmad, M.N. Catalyst Design for Dry Reforming of Methane: Analysis Review. *Renew. Sustain. Energy Rev.* **2018**, *82*, 2570–2585. [CrossRef]
17. Gao, Y.; Jiang, J.; Meng, Y.; Yan, F.; Aihemaiti, A. A Review of Recent Developments in Hydrogen Production via Biogas Dry Reforming. *Energy Convers. Manag.* **2018**, *171*, 133–155. [CrossRef]

18. Han, B.; Wang, F.; Zhang, L.; Wang, Y.; Fan, W.; Xu, L.; Yu, H.; Li, Z. Syngas Production from Methane Steam Reforming and Dry Reforming Reactions over Sintering−Resistant Ni@SiO_2 Catalyst. *Res. Chem. Intermed.* **2020**, *46*, 1735–1748. [CrossRef]
19. Manan, W.N.; Wan Isahak, W.N.R.; Yaakob, Z. CeO_2−Based Heterogeneous Catalysts in Dry Reforming Methane and Steam Reforming Methane: A Short Review. *Catalysts* **2022**, *12*, 452. [CrossRef]
20. Chaghouri, M.; Hany, S.; Cazier, F.; Tidahy, H.L.; Gennequin, C.; Abi−Aad, E. Impact of Impurities on Biogas Valorization through Dry Reforming of Methane Reaction. *Int. J. Hydrogen Energy* **2022**, *47*, 40415–40429. [CrossRef]
21. Phan, T.S.; Pham Minh, D. New Performing Hydroxyapatite−Based Catalysts in Dry−Reforming of Methane. *Int. J. Hydrogen Energy* **2023**, *48*, 30770–30790. [CrossRef]
22. Haug, L.; Thurner, C.; Bekheet, M.F.; Ploner, K.; Bischoff, B.; Gurlo, A.; Kunz, M.; Sartory, B.; Penner, S.; Klötzer, B. Pivotal Role of Ni/ZrO_2 Phase Boundaries for Coke-Resistant Methane Dry Reforming Catalysts. *Catalysts* **2023**, *13*, 804. [CrossRef]
23. Wang, K.; Ren, X.; Yin, G.; Hu, E.; Zhang, H. Recent Advances in Plasma−Based Methane Reforming for Syngas Production. *Curr. Opin. Green Sustain. Chem.* **2024**, *50*, 100981. [CrossRef]
24. Fan, L.; Li, C.; van Biert, L.; Zhou, S.-H.; Tabish, A.N.; Mokhov, A.; Aravind, P.V.; Cai, W. Advances on Methane Reforming in Solid Oxide Fuel Cells. *Renew. Sustain. Energy Rev.* **2022**, *166*, 112646. [CrossRef]
25. Liu, Z.; Xu, B.; Jiang, Y.J.; Zhou, Y.; Sun, X.; Wang, Y.; Zhu, W. Photocatalytic Conversion of Methane: Current State of the Art, Challenges, and Future Perspectives. *ACS Environ. Au* **2023**, *3*, 252–276. [CrossRef]
26. Ahasan, M.R.; Hossain, M.M.; Ding, X.; Wang, R. Non−Equilibrium Plasma−Assisted Dry Reforming of Methane over Shape−Controlled CeO_2 Supported Ruthenium Catalysts. *J. Mater. Chem. A* **2023**, *11*, 10993–11009. [CrossRef]
27. Xu, Y.; Liu, N.; Lin, Y.; Mao, X.; Zhong, H.; Chang, Z.; Shneider, M.N.; Ju, Y. Enhancements of Electric Field and Afterglow of Non−Equilibrium Plasma by $Pb(Zr_xTi_{1-x})O_3$ Ferroelectric Electrode. *Nat. Commun.* **2024**, *15*, 3092. [CrossRef]
28. Beil, S.B.; Bonnet, S.; Casadevall, C.; Detz, R.J.; Eisenreich, F.; Glover, S.D.; Kerzig, C.; Næsborg, L.; Pullen, S.; Storch, G.; et al. Challenges and Future Perspectives in Photocatalysis: Conclusions from an Interdisciplinary Workshop. *JACS Au* **2024**, *4*, 2746–2766. [CrossRef] [PubMed]
29. Mishra, S.; Sundaram, B. A Review of the Photocatalysis Process Used for Wastewater Treatment. *Mater. Today Proc.* **2024**, *102*, 393–409. [CrossRef]
30. Kobielusz, M.; Mikrut, P.; Macyk, W. Photocatalytic Synthesis of Chemicals. In *Materials for Sustainable Energy. Advances in Inorganic Chemistry*; van Eldik, R., Macyk, W., Eds.; Elsevier: Amsterdam, The Netherlands, 2018; Volume 72, pp. 93–144, ISBN 978-0-12-815077-1.
31. Yao, Y.; Gao, X.; Li, Z.; Meng, X. Photocatalytic Reforming for Hydrogen Evolution: A Review. *Catalysts* **2020**, *10*, 335. [CrossRef]
32. Shoji, S.; Peng, X.; Yamaguchi, A.; Watanabe, R.; Fukuhara, C.; Cho, Y.; Yamamoto, T.; Matsumura, S.; Yu, M.W.; Ishii, S.; et al. Photocatalytic Uphill Conversion of Natural Gas beyond the Limitation of Thermal Reaction Systems. *Nat. Catal.* **2020**, *3*, 148–153. [CrossRef]
33. Zhang, L.; Kuang, P.; Yu, J. Introductory Chapter: Fundamentals of Photocatalysis and Electrocatalysis. In *Graphene Oxide−Metal Oxide and other Graphene Oxide−Based Composites in Photocatalysis and Electrocatalysis*; Jiaguo, Y., Liuyang, Z., Panyong, K., Eds.; Elsevier: Amsterdam, The Netherlands, 2022; pp. 1–30.
34. Lian, H.-Y.; Li, X.-S.; Liu, J.-L.; Zhu, X.; Zhu, A.-M. Oxidative Pyrolysis Reforming of Methanol in Warm Plasma for an On−Board Hydrogen Production. *Int. J. Hydrogen Energy* **2017**, *42*, 13617–13624. [CrossRef]
35. Cvetinović, D.; Erić, A.; Anđelković, J.; Ćetenović, N.; Jovanović, M.; Bakić, V. Economic Viability of Hydrogen Production via Plasma Thermal Degradation of Natural Gas. *Processes* **2025**, *13*, 1888. [CrossRef]
36. Escribà−Gelonch, M.; Osorio−Tejada, J.; Yu, L.; Wanten, B.; Bogaerts, A.; Hessel, V. Techno−Economic and Life−Cycle Assessment for Syngas Production Using Sustainable Plasma−Assisted Methane Reforming Technologies. *Energy Environ. Sci.* **2025**, *18*, 6043–6062. [CrossRef]
37. Ameta, R.; Solanki, M.S.; Benjamin, S.; Ameta, S.C. Photocatalysis. In *Advanced Oxidation Processes for Waste Water Treatment*; Elsevier: Amsterdam, The Netherlands, 2018; pp. 135–175.
38. Yang, X.; Wang, D. Photocatalysis: From Fundamental Principles to Materials and Applications. *ACS Appl. Energy Mater.* **2018**, *1*, 6657–6693. [CrossRef]
39. Li, Z.; Yi, Z.; Li, Z.; Zou, Z. Photocatalytic and Thermocatalytic Conversion of Methane. *Sol. RRL* **2021**, *5*, 2000596. [CrossRef]
40. Song, H.; Ye, J. Direct Photocatalytic Conversion of Methane to Value−Added Chemicals. *Trends Chem.* **2022**, *4*, 1094–1105. [CrossRef]
41. Cho, Y.; Yamaguchi, A.; Miyauchi, M. Photocatalytic Methane Reforming: Recent Advances. *Catalysts* **2020**, *11*, 18. [CrossRef]
42. Kulandaivalu, T.; Mohamed, A.R.; Ali, K.A.; Mohammadi, M. Photocatalytic Carbon Dioxide Reforming of Methane as an Alternative Approach for Solar Fuel Production−a Review. *Renew. Sustain. Energy Rev.* **2020**, *134*, 110363. [CrossRef]
43. Wang, P.; Shi, R.; Zhao, J.; Zhang, T. Photodriven Methane Conversion on Transition Metal Oxide Catalyst: Recent Progress and Prospects. *Adv. Sci.* **2024**, *11*, e2305471. [CrossRef]

44. Lei, Y.; Sala, X.; García−Antón, J.; Muñoz, J. A Review on Photocatalytic Methane Conversion Systems: From Fundamental Mechanisms to the Emerging Role of Ferroelectric Materials. *J. Mater. Chem. A* **2025**, *13*, 12712–12745. [CrossRef]
45. Xu, S.; Huang, X.; Lu, H. Photocatalytic Reforming of Biomass for Hydrogen Production: A Comprehensive Overview. *Fuel Process. Technol.* **2024**, *255*, 108057. [CrossRef]
46. Pan, H.; Li, J.; Wang, Y.; Xia, Q.; Qiu, L.; Zhou, B. Solar−driven Biomass Reforming for Hydrogen Generation: Principles, Advances, and Challenges. *Adv. Sci.* **2024**, *11*, e2402651. [CrossRef] [PubMed]
47. Yang, G.; Xu, Q.; Zeng, G. Developments of Photo−/Electro−catalysis Based on Covalent Organic Frameworks: A Review. *Electron* **2024**, *2*, e39. [CrossRef]
48. Sahu, J.; Prusty, D.; Mansingh, S.; Parida, K. A Review on Alloyed Quantum Dots and Their Applications as Photocatalysts. *Int. J. Hydrogen Energy* **2023**, *48*, 29097–29118. [CrossRef]
49. Luo, J.; Selopal, G.S.; Tong, X.; Wang, Z. Colloidal Quantum Dots and Two−dimensional Material Heterostructures for Photodetector Applications. *Electron* **2024**, *2*, e30. [CrossRef]
50. Yang, H. A Short Review on Heterojunction Photocatalysts: Carrier Transfer Behavior and Photocatalytic Mechanisms. *Mater. Res. Bull.* **2021**, *142*, 111406. [CrossRef]
51. Jiang, Y.; Li, S.; Fan, Y.; Tang, Z. Best Practices for Experiments and Reports in Photocatalytic Methane Conversion. *Angew. Chem. Int. Ed.* **2024**, *63*, e202404658. [CrossRef]
52. Khodadadian, F.; de Boer, M.W.; Poursaeidesfahani, A.; van Ommen, J.R.; Stankiewicz, A.I.; Lakerveld, R. Design, Characterization and Model Validation of a LED−Based Photocatalytic Reactor for Gas Phase Applications. *Chem. Eng. J.* **2018**, *333*, 456–466. [CrossRef]
53. Wang, D.; Mueses, M.A.; Márquez, J.A.C.; Machuca−Martínez, F.; Grčić, I.; Peralta Muniz Moreira, R.; Li Puma, G. Engineering and Modeling Perspectives on Photocatalytic Reactors for Water Treatment. *Water Res.* **2021**, *202*, 117421. [CrossRef]
54. Sundar, K.P.; Kanmani, S. Progression of Photocatalytic Reactors and It's Comparison: A Review. *Chem. Eng. Res. Des.* **2020**, *154*, 135–150. [CrossRef]
55. Binjhade, R.; Mondal, R.; Mondal, S. Continuous Photocatalytic Reactor: Critical Review on the Design and Performance. *J. Environ. Chem. Eng.* **2022**, *10*, 107746. [CrossRef]
56. Zhu, Z.; Guo, W.; Zhang, Y.; Pan, C.; Xu, J.; Zhu, Y.; Lou, Y. Research Progress on Methane Conversion Coupling Photocatalysis and Thermocatalysis. *Carbon Energy* **2021**, *3*, 519–540. [CrossRef]
57. Li, M.; Sun, Z.; Hu, Y.H. Thermo−Photo Coupled Catalytic CO_2 Reforming of Methane: A Review. *Chem. Eng. J.* **2022**, *428*, 131222. [CrossRef]
58. Tavasoli, A.V.; Preston, M.; Ozin, G. Photocatalytic Dry Reforming: What Is It Good For? *Energy Environ. Sci.* **2021**, *14*, 3098–3109. [CrossRef]
59. Kisch, H. Semiconductor Photocatalysis—Mechanistic and Synthetic Aspects. *Angew. Chem. Int. Ed.* **2013**, *52*, 812–847. [CrossRef]
60. Wang, L.; Yu, J. Chapter 1−Principles of Photocatalysis. In *S−Scheme Heterojunction Photocatalysts: Fundamentals and Applications. Interface Science and Technology*; Yu, J., Zhang, L., Wang, L., Zhu, B., Eds.; Elsevier: Amsterdam, The Netherlands, 2023; Volume 35, pp. 1–52.
61. Ayyub, M.M.; Rao, C.N.R. Design of Efficient Photocatalysts through Band Gap Engineering. In *Nanostructured Photocatalysts−From Materials to Applications in Solar Fuels and Environmental Remediation*; Boukherroub, R., Robertson, N., Eds.; Elsevier: Amsterdam, The Netherlands, 2020; pp. 1–18.
62. Tuama, A.N.; Alzubaidi, L.H.; Jameel, M.H.; Abass, K.H.; bin Mayzan, M.Z.H.; Salman, Z.N. Impact of Electron–Hole Recombination Mechanism on the Photocatalytic Performance of ZnO in Water Treatment: A Review. *J. Sol.−Gel. Sci. Technol.* **2024**, *110*, 792–806. [CrossRef]
63. Yuan, J.; Li, H.; Wang, G.; Zhang, C.; Wang, Y.; Yang, L.; Li, M.; Lu, J. Adsorption, Isolated Electron/Hole Transport, and Confined Catalysis Coupling to Enhance the Photocatalytic Degradation Performance. *Appl. Catal. B Environ.* **2022**, *303*, 120892. [CrossRef]
64. Tu, H.; Tian, B.; Chen, S.; Xu, J.; Yang, J.; Zhao, Z.; Chen, S.; Wu, J. Enhancing Photocatalytic Efficiency through Surface Modification to Manipulate Internal Electron−Hole Distribution. *NPJ Clean Water* **2025**, *8*, 48. [CrossRef]
65. Akhter, P.; Arshad, A.; Saleem, A.; Hussain, M. Recent Development in Non−Metal−Doped Titanium Dioxide Photocatalysts for Different Dyes Degradation and the Study of Their Strategic Factors: A Review. *Catalysts* **2022**, *12*, 1331. [CrossRef]
66. Fang, W.; Yan, J.; Wei, Z.; Liu, J.; Guo, W.; Jiang, Z.; Shangguan, W. Account of Doping Photocatalyst for Water Splitting. *Chin. J. Catal.* **2024**, *60*, 1–24. [CrossRef]
67. Flores, N.M.; Pal, U.; Galeazzi, R.; Sandoval, A. Effects of Morphology, Surface Area, and Defect Content on the Photocatalytic Dye Degradation Performance of ZnO Nanostructures. *RSC Adv.* **2014**, *4*, 41099–41110. [CrossRef]
68. Wang, Z.; Xiao, M.; You, J.; Liu, G.; Wang, L. Defect Engineering in Photocatalysts and Photoelectrodes: From Small to Big. *Acc. Mater. Res.* **2022**, *3*, 1127–1136. [CrossRef]
69. Yu, Y.; Zhang, P.; Guo, L.; Chen, Z.; Wu, Q.; Ding, Y.; Zheng, W.; Cao, Y. The Design of TiO_2 Nanostructures (Nanoparticle, Nanotube, and Nanosheet) and Their Photocatalytic Activity. *J. Phys. Chem. C* **2014**, *118*, 12727–12733. [CrossRef]

70. Gao, P.; Li, A.; Sun, D.D.; Ng, W.J. Effects of Various TiO_2 Nanostructures and Graphene Oxide on Photocatalytic Activity of TiO_2. *J. Hazard. Mater.* **2014**, *279*, 96–104. [CrossRef]
71. Lincho, J.; Zaleska−Medynska, A.; Martins, R.C.; Gomes, J. Nanostructured Photocatalysts for the Abatement of Contaminants by Photocatalysis and Photocatalytic Ozonation: An Overview. *Sci. Total Environ.* **2022**, *837*, 155776. [CrossRef] [PubMed]
72. Zhou, S.; Li, H.; Gao, H.; Li, A.; Li, T.; Cheng, S.; Wang, J.; Kasemchainan, J.; Yi, J.; Zhao, F.; et al. Recent Advances in Metal−Loaded MOFs Photocatalysts: From Single Atom, Cluster to Nanoparticle. *Chin. Chem. Lett.* **2024**, *36*, 110142. [CrossRef]
73. Hamdan, S.; Wigglesworth, M.J.; Muscetta, M.; Ma, R.; Helal, M.I.; Martsinovich, N.; Palmisano, G.; Vernuccio, S. Unravelling the Photoactivity of Metal−Loaded TiO_2 for Hydrogen Production: Insights from a Combined Experimental and Computational Analysis. *Int. J. Hydrogen Energy* **2025**, *118*, 394–406. [CrossRef]
74. Balapure, A.; Ray Dutta, J.; Ganesan, R. Recent Advances in Semiconductor Heterojunctions: A Detailed Review of the Fundamentals of Photocatalysis, Charge Transfer Mechanism and Materials. *RSC Appl. Interfaces* **2024**, *1*, 43–69. [CrossRef]
75. Low, J.; Yu, J.; Jaroniec, M.; Wageh, S.; Al−Ghamdi, A.A. Heterojunction Photocatalysts. *Adv. Mater.* **2017**, *29*, 1601694. [CrossRef]
76. Salazar−Marín, D.; Oza, G.; Real, J.A.D.; Cervantes−Uribe, A.; Pérez−Vidal, H.; Kesarla, M.K.; Torres, J.G.T.; Godavarthi, S. Distinguishing between Type II and S−Scheme Heterojunction Materials: A Comprehensive Review. *Appl. Surf. Sci. Adv.* **2024**, *19*, 100536. [CrossRef]
77. Yuan, Y.; Guo, R.; Hong, L.; Ji, X.; Lin, Z.; Li, Z.; Pan, W. A Review of Metal Oxide−Based Z−Scheme Heterojunction Photocatalysts: Actualities and Developments. *Mater. Today Energy* **2021**, *21*, 100829. [CrossRef]
78. Kumari, P.; Bahadur, N.; Kong, L.; O'Dell, L.A.; Merenda, A.; Dumée, L.F. Engineering Schottky−like and Hetero−junction Materials for Enhanced Photocatalysis Performance—A Review. *Mater Adv.* **2022**, *3*, 2309–2323. [CrossRef]
79. Rao, V.N.; Reddy, N.L.; Kumari, M.M.; Cheralathan, K.K.; Ravi, P.; Sathish, M.; Neppolian, B.; Reddy, K.R.; Shetti, N.P.; Prathap, P.; et al. Sustainable Hydrogen Production for the Greener Environment by Quantum Dots−Based Efficient Photocatalysts: A Review. *J. Environ. Manag.* **2019**, *248*, 109246. [CrossRef]
80. Sun, P.; Xing, Z.; Li, Z.; Zhou, W. Recent Advances in Quantum Dots Photocatalysts. *Chem. Eng. J.* **2023**, *458*, 141399. [CrossRef]
81. Schneider, J.; Matsuoka, M.; Takeuchi, M.; Zhang, J.; Horiuchi, Y.; Anpo, M.; Bahnemann, D.W. Understanding TiO_2 Photocatalysis: Mechanisms and Materials. *Chem. Rev.* **2014**, *114*, 9919–9986. [CrossRef]
82. Dharma, H.N.C.; Jaafar, J.; Widiastuti, N.; Matsuyama, H.; Rajabsadeh, S.; Othman, M.H.D.; Rahman, M.A.; Jafri, N.N.M.; Suhaimin, N.S.; Nasir, A.M.; et al. A Review of Titanium Dioxide (TiO_2)−Based Photocatalyst for Oilfield−Produced Water Treatment. *Membranes* **2022**, *12*, 345. [CrossRef] [PubMed]
83. Arun, J.; Nachiappan, S.; Rangarajan, G.; Alagappan, R.P.; Gopinath, K.P.; Lichtfouse, E. Synthesis and Application of Titanium Dioxide Photocatalysis for Energy, Decontamination and Viral Disinfection: A Review. *Environ. Chem. Lett.* **2023**, *21*, 339–362. [CrossRef]
84. Martín−Sómer, M.; Pablos, C.; van Grieken, R.; Marugán, J. Influence of Light Distribution on the Performance of Photocatalytic Reactors: LED vs. Mercury Lamps. *Appl. Catal. B Environ.* **2017**, *215*, 1–7. [CrossRef]
85. Masoud, N.M.; Murnick, D.E. High Efficiency Fluorescent Excimer Lamps: An Alternative to Mercury Based UVC Lamps. *Rev. Sci. Instrum.* **2013**, *84*, 123108. [CrossRef]
86. Hölz, K.; Lietard, J.; Somoza, M.M. High−Power 365 Nm UV LED Mercury Arc Lamp Replacement for Photochemistry and Chemical Photolithography. *ACS Sustain. Chem. Eng.* **2017**, *5*, 828–834. [CrossRef]
87. Pelayo, D.; Rivero, M.J.; Santos, G.; Gómez, P.; Ortiz, I. Techno−Economic Evaluation of UV Light Technologies in Water Remediation. *Sci. Total Environ.* **2023**, *868*, 161376. [CrossRef]
88. Rehman, S.; Ullah, R.; Butt, A.M.; Gohar, N.D. Strategies of Making TiO_2 and ZnO Visible Light Active. *J. Hazard. Mater.* **2009**, *170*, 560–569. [CrossRef] [PubMed]
89. Kumar, S.G.; Devi, L.G. Review on Modified TiO_2 Photocatalysis under UV/Visible Light: Selected Results and Related Mechanisms on Interfacial Charge Carrier Transfer Dynamics. *J. Phys. Chem. A* **2011**, *115*, 13211–13241. [CrossRef] [PubMed]
90. Hashemizadeh, I.; Golovko, V.B.; Choi, J.; Tsang, D.C.W.; Yip, A.C.K. Photocatalytic Reduction of CO_2 to Hydrocarbons Using Bio−Templated Porous TiO_2 Architectures under UV and Visible Light. *Chem. Eng. J.* **2018**, *347*, 64–73. [CrossRef]
91. Al Zoubi, W.; Salih Al−Hamdani, A.A.; Sunghun, B.; Ko, Y.G. A Review on TiO_2−Based Composites for Superior Photocatalytic Activity. *Rev. Inorg. Chem.* **2021**, *41*, 213–222. [CrossRef]
92. Arora, I.; Chawla, H.; Chandra, A.; Sagadevan, S.; Garg, S. Advances in the Strategies for Enhancing the Photocatalytic Activity of TiO_2: Conversion from UV−Light Active to Visible−Light Active Photocatalyst. *Inorg. Chem. Commun.* **2022**, *143*, 109700. [CrossRef]
93. Tinoco Navarro, L.K.; Jaroslav, C. Enhancing Photocatalytic Properties of TiO_2 Photocatalyst and Heterojunctions: A Comprehensive Review of the Impact of Biphasic Systems in Aerogels and Xerogels Synthesis, Methods, and Mechanisms for Environmental Applications. *Gels* **2023**, *9*, 976. [CrossRef]
94. Chauke, N.M.; Mohlala, R.L.; Ngqoloda, S.; Raphulu, M.C. Harnessing Visible Light: Enhancing TiO_2 Photocatalysis with Photosensitizers for Sustainable and Efficient Environmental Solutions. *Front. Chem. Eng.* **2024**, *6*, 1356021. [CrossRef]

95. Acharya, R.; Pani, P. Visible Light Susceptible Doped TiO_2 Photocatalytic Systems: An Overview. *Mater. Today Proc.* **2022**, *67*, 1276–1282. [CrossRef]
96. Prakash, J.; Sun, S.; Swart, H.C.; Gupta, R.K. Noble Metals−TiO_2 Nanocomposites: From Fundamental Mechanisms to Photocatalysis, Surface Enhanced Raman Scattering and Antibacterial Applications. *Appl. Mater. Today* **2018**, *11*, 82–135. [CrossRef]
97. Yadav, M.; Basheer, H.S.; Ágfalvi, Á.; Ábrahámné, K.B.; Kiss, J.; Halasi, G.; Sápi, A.; Kukovecz, Á.; Kónya, Z. Noble Metals−Deposited TiO_2 Photocatalysts for Photoreduction of CO_2: Exploration of Surface Chemistry and a Reflection on the Importance of Wavelength Dependence. *Appl. Catal. A Gen.* **2023**, *668*, 119434. [CrossRef]
98. Blanco−Vega, M.P.; Guzmán−Mar, J.L.; Villanueva−Rodríguez, M.; Maya−Treviño, L.; Garza−Tovar, L.L.; Hernández−Ramírez, A.; Hinojosa−Reyes, L. Photocatalytic Elimination of Bisphenol A under Visible Light Using Ni−Doped TiO_2 Synthesized by Microwave Assisted Sol−Gel Method. *Mater. Sci. Semicond. Process.* **2017**, *71*, 275–282. [CrossRef]
99. Baruah, M.; Ezung, S.L.; Sharma, S.; Bora Sinha, U.; Sinha, D. Synthesis and Characterization of Ni−Doped TiO_2 Activated Carbon Nanocomposite for the Photocatalytic Degradation of Anthracene. *Inorg. Chem. Commun.* **2022**, *144*, 109905. [CrossRef]
100. Sood, S.; Umar, A.; Mehta, S.K.; Kansal, S.K. Highly Effective Fe−Doped TiO_2 Nanoparticles Photocatalysts for Visible−Light Driven Photocatalytic Degradation of Toxic Organic Compounds. *J. Colloid Interface Sci.* **2015**, *450*, 213–223. [CrossRef] [PubMed]
101. Moradi, V.; Jun, M.B.G.; Blackburn, A.; Herring, R.A. Significant Improvement in Visible Light Photocatalytic Activity of Fe Doped TiO_2 Using an Acid Treatment Process. *Appl. Surf. Sci.* **2018**, *427*, 791–799. [CrossRef]
102. Khalid, N.R.; Ahmed, E.; Hong, Z.; Ahmad, M.; Zhang, Y.; Khalid, S. Cu−Doped TiO_2 Nanoparticles/Graphene Composites for Efficient Visible−Light Photocatalysis. *Ceram. Int.* **2013**, *39*, 7107–7113. [CrossRef]
103. Clarizia, L.; Spasiano, D.; Di Somma, I.; Marotta, R.; Andreozzi, R.; Dionysiou, D.D. Copper Modified−TiO_2 Catalysts for Hydrogen Generation through Photoreforming of Organics. A Short Review. *Int. J. Hydrogen Energy* **2014**, *39*, 16812–16831. [CrossRef]
104. Iwasaki, M.; Hara, M.; Kawada, H.; Tada, H.; Ito, S. Cobalt Ion−Doped TiO_2 Photocatalyst Response to Visible Light. *J. Colloid Interface Sci.* **2000**, *224*, 202–204. [CrossRef]
105. Binas, V.D.; Sambani, K.; Maggos, T.; Katsanaki, A.; Kiriakidis, G. Synthesis and Photocatalytic Activity of Mn−Doped TiO_2 Nanostructured Powders under UV and Visible Light. *Appl. Catal. B Environ.* **2012**, *113–114*, 79–86. [CrossRef]
106. Sudrajat, H.; Babel, S.; Ta, A.T.; Nguyen, T.K. Mn−Doped TiO_2 Photocatalysts: Role, Chemical Identity, and Local Structure of Dopant. *J. Phys. Chem. Solids* **2020**, *144*, 109517. [CrossRef]
107. Xie, J.; Jiang, D.; Chen, M.; Li, D.; Zhu, J.; Lü, X.; Yan, C. Preparation and Characterization of Monodisperse Ce−Doped TiO_2 Microspheres with Visible Light Photocatalytic Activity. *Colloids Surf. A Physicochem. Eng. Asp.* **2010**, *372*, 107–114. [CrossRef]
108. Tahir, B.; Tahir, M.; Amin, N.A.S. Tailoring Performance of La−Modified TiO_2 Nanocatalyst for Continuous Photocatalytic CO_2 Reforming of CH_4 to Fuels in the Presence of H_2O. *Energy Convers. Manag.* **2018**, *159*, 284–298. [CrossRef]
109. Yamaguchi, A.; Kujirai, T.; Fujita, T.; Abe, H.; Miyauchi, M. Steam Reforming of Methane by Titanium Oxide Photocatalysts with Hollow Spheres. *Sustain. Energy Fuels* **2024**, *8*, 516–523. [CrossRef]
110. Al−Madanat, O.; Alsalka, Y.; Curti, M.; Dillert, R.; Bahnemann, D.W. Mechanistic Insights into Hydrogen Evolution by Photocatalytic Reforming of Naphthalene. *ACS Catal.* **2020**, *10*, 7398–7412. [CrossRef]
111. Genco, A.; García−López, E.I.; Megna, B.; Ania, C.; Marcì, G. Nb_2O_5 Based Photocatalysts for Efficient Generation of H_2 by Photoreforming of Aqueous Solutions of Ethanol. *Catal. Today* **2025**, *447*, 115147. [CrossRef]
112. Eisapour, M.; Huang, R.; Roostaei, T.; Zhao, H.; Hu, J.; Chen, Z. Sandwich−like Heterojunction of NiO−Ni−TiO_2 for Simultaneous Production of Hydrogen and Value−Added Products from Glycerol Photoreforming. *Environ. Surf. Interfaces* **2025**, *3*, 46–54. [CrossRef]
113. Liu, J.; Zhou, Y.; Fan, Y.; Sun, X.; Qiao, P.; Xiao, X.; Zhang, Q.; Tian, C.; Jiang, B. Regulating the Local Electronic Structure by Constructing Ni–O–Ni Sites Confined in TiO_2 for Selective Photocatalytic Glycerol Reforming. *J. Energy Chem.* **2025**, *108*, 129–137. [CrossRef]
114. Xie, T.; Zhang, Z.-Y.; Zheng, H.-Y.; Xu, K.-D.; Hu, Z.; Lei, Y. Enhanced Photothermal Catalytic Performance of Dry Reforming of Methane over Ni/Mesoporous TiO_2 Composite Catalyst. *Chem. Eng. J.* **2022**, *429*, 132507. [CrossRef]
115. He, Z.; Gong, K.; Dai, Y.; Niu, Q.; Lin, T.; Zhong, L. Regulating Crystal Phase of TiO_2 to Enhance Catalytic Activity of Ni/TiO_2 for Solar−Driven Dry Reforming of Methane. *J. Fuel Chem. Technol.* **2024**, *52*, 1203–1213. [CrossRef]
116. Belda−Marco, S.; Ayala, P.; Myakala, S.N.; Eder, D.; Lillo−Ródenas, M.Á.; Cherevan, A.; Román−Martínez, M.C. Production of H_2 and Organic Acids by Cellulose Photo−Reforming with TiO_2−Bimetallic (CuNi) Co−Catalysts: Metal Loading and Photodeposition Sequence Effects. *Environ. Res.* **2025**, *271*, 121141. [CrossRef]
117. Muscetta, M.; Clarizia, L.; Race, M.; Andreozzi, R.; Marotta, R.; Di Somma, I. Visible−Light Driven Systems: Effect of the Parameters Affecting Hydrogen Production through Photoreforming of Organics in Presence of Cu_2O/TiO_2 Nanocomposite Photocatalyst. *Appl. Sci.* **2023**, *13*, 2337. [CrossRef]

118. Umair, M.; Ruiz−Aguirre, A.; Berruti, I.; Rodríguez, S.M.; Palmisano, L.; Loddo, V.; Bellardita, M. Biomass Derivatives Photoreforming in Pilot Plant Scale to Obtain H_2 under Green Conditions by Using Ball Milling Cu_2O−TiO_2 P25 Photocatalysts. *Chem. Eng. J.* **2025**, *504*, 158585. [CrossRef]
119. Khan, A.; Le Pivert, M.; Ranjbari, A.; Dragoe, D.; Bahena−Uribe, D.; Colbeau−Justin, C.; Herrero, C.; Rutkowska−Zbik, D.; Deschamps, J.; Remita, H. Cu−Based MOF/TiO_2 Composite Nanomaterials for Photocatalytic Hydrogen Generation and the Role of Copper. *Adv. Funct. Mater.* **2025**, *2021*. [CrossRef]
120. Qian, H.; Yuan, B.; Liu, Y.; Wang, L.; Zhu, R.; Dong, P. Effect of Cu Valence States on Conduction Band Position and Reduction Selectivity of TiO_2−Based Heterojunction Photocatalysts. *iScience* **2025**, *28*, 112697. [CrossRef]
121. Belda−Marco, S.; Lillo−Ródenas, M.Á.; Román−Martínez, M.C. Optimization of Active Sites in TiO_2−Cu Photocatalysts for H_2 Generation via Cellulose Photo−Reforming. *ChemCatChem* **2025**, *17*, e202500250. [CrossRef]
122. Liu, X.; Bao, C.; Zhu, Z.; Zheng, H.; Song, C.; Xu, Q. Thermo−Photo Synergic Effect on Methanol Steam Reforming over Mesoporous Cu/TiO_2–CeO_2 Catalysts. *Int. J. Hydrogen Energy* **2021**, *46*, 26741–26756. [CrossRef]
123. Fan, H.; Su, J.; Zhao, E.; Zheng, Y.; Chen, Z. Photocatalytic Selective Oxidation of Glycerol to Formic Acid and Formaldehyde over Surface Cobalt−Doped Titanium Dioxide. *J. Colloid Interface Sci.* **2025**, *684*, 140–147. [CrossRef]
124. Pei, M.; Zhang, M.; Tian, J.; Yang, Y.; Liu, E. Photocatalytic H_2 Production over $CoxNi_{0.85-x}Se$ Decorated TiO_2 S−Scheme Heterojunction. *J. Alloys Compd.* **2025**, *1010*, 177266. [CrossRef]
125. Ayodele, B.V.; Ghazali, A.A.; Mohd Yassin, M.Y.; Abdullah, S. Optimization of Hydrogen Production by Photocatalytic Steam Methane Reforming over Lanthanum Modified Titanium (IV) Oxide Using Response Surface Methodology. *Int. J. Hydrogen Energy* **2019**, *44*, 20700–20710. [CrossRef]
126. Zhang, Z.; Zhang, Y.; Han, C.; Yan, M.; Ji, G.; Wang, W. Efficient Photo−Oxidation of C(Sp3)−H Bonds on Visible−Light−Responsive W−Doped TiO_2 Nanocrystals Promoted by the Photochromic Effect. *Inorg. Chem. Front.* **2025**. [CrossRef]
127. Hu, Y.H.; Wang, J.H.; Chen, Y.; Tang, J.P.; Wang, Z.Y.; Yuan, Y.J. Solar Driven Conversion of Agricultural Biomass to H_2 over Few−Layer MoS_2 Modified Ultra−Small TiO_2 Nanoparticle Photocatalysts. *J. Mater. Chem. A* **2025**, *13*, 13402–13409. [CrossRef]
128. Falara, P.P.; Chatzikonstantinou, N.; Zourou, A.; Tsipas, P.; Sakellis, E.; Alexandratou, E.; Nasikas, N.K.; Kordatos, K.V.; Antoniadou, M. Optimizing Carbon Dot−TiO_2 Nanohybrids for Enhanced Photocatalytic Hydrogen Evolution. *Materials* **2025**, *18*, 1023. [CrossRef] [PubMed]
129. Udaibah, W.; Anggoro, D.D.; Prasetyaningrum, A.; Bafaqeer, A.; Amin, N.A.S. An Enhanced Production of Biomethane from Cellulose Photoreforming Driven by Titania Morphological Modification. *React. Kinet. Mech. Catal.* **2025**, *138*, 1–17. [CrossRef]
130. Jiang, Y.; Zhao, W.; Li, S.; Wang, S.; Fan, Y.; Wang, F.; Qiu, X.; Zhu, Y.; Zhang, Y.; Long, C.; et al. Elevating Photooxidation of Methane to Formaldehyde via TiO_2 Crystal Phase Engineering. *J. Am. Chem. Soc.* **2022**, *144*, 15977–15987. [CrossRef] [PubMed]
131. Zhang, C.; Wang, J.; Che, L.; Shi, L. Crystal Phase Engineering of TiO_2 for Efficient Photocatalytic Non−Oxidative Methane Coupling. *Chem. Eur. J.* **2025**, *31*, e202500216. [CrossRef]
132. Sun, J.; Wang, Q.; Wang, W.; Wang, K. Study on the Synergism of Steam Reforming and Photocatalysis for the Degradation of Toluene as a Tar Model Compound under Microwave−Metal Discharges. *Energy* **2018**, *155*, 815–823. [CrossRef]
133. Aldeen, E.M.S.; Jalil, A.A.; Mim, R.S.; Alhebshi, A.; Hassan, N.S.; Saravanan, R. Altered Zirconium Dioxide Based Photocatalyst for Enhancement of Organic Pollutants Degradation: A Review. *Chemosphere* **2022**, *304*, 135349. [CrossRef]
134. Rani, V.; Sharma, A.; Kumar, A.; Singh, P.; Thakur, S.; Singh, A.; Van Le, Q.; Nguyen, V.H.; Raizada, P. ZrO_2−Based Photocatalysts for Wastewater Treatment: From Novel Modification Strategies to Mechanistic Insights. *Catalysts* **2022**, *12*, 1418. [CrossRef]
135. Tian, Y.; Li, Y.; Cao, D.; Liu, Q.; Cai, W. Photothermal Dry Reforming of Ethanol over Rod−like Ni/ZrO_2 Catalysts. *Mol. Catal.* **2024**, *564*, 114308. [CrossRef]
136. Du, Z.; Pan, F.; Yang, X.; Fang, L.; Gang, Y.; Fang, S.; Li, T.; Hu, Y.H.; Li, Y. Efficient Photothermochemical Dry Reforming of Methane over Ni Supported on ZrO_2 with CeO_2 Incorporation. *Catal. Today* **2023**, *409*, 31–41. [CrossRef]
137. Cheng, J.; Liu, X.; Li, T.; Li, D.; Jiang, Z.; Xu, D.; Patel, B.; Guo, Y. Ce Doping Boosted Photothermal Synergistic Catalytic Reforming of CH_4 and CO_2 into Syngas over Ni/ZrO_2 at Medium−Low Temperature. *Int. J. Hydrogen Energy* **2024**, *53*, 1433–1444. [CrossRef]
138. Tengfei, L.; Cheng, J.; Li, D.; Xu, D.; Patel, B.; Guo, Y. Syngas Production from Photothermal Synergistic Dry Reforming of CH_4 over a Core−Shell Structured Ni/CeO_2–ZrO_2@SiO_2 Catalyst. *Int. J. Hydrogen Energy* **2024**, *67*, 1194–1205. [CrossRef]
139. Liu, Y.; Liu, X.; Li, D.; Li, T.; Guo, Y. Tailored Interfaces Promoting Photo−Activation of Molecular Enclosed CO_2 on MOF−Derived Ni/$CeZrO_2$ for Photothermal Synergistic Dry Reforming of Methane. *Chem. Eng. J.* **2025**, *512*, 162499. [CrossRef]
140. Meng, L.; Jia, Y.; Wu, S. Efficient Photothermal Catalytic Methane Dry Reforming over Rich Oxygen Vacancy Catalysts. *ChemComm* **2025**, *61*, 2301–2304. [CrossRef]
141. García−Mendoza, C.; Oros−Ruiz, S.; Ramírez−Rave, S.; Morales−Mendoza, G.; López, R.; Gómez, R. Synthesis of Bi_2S_3 Nanorods Supported on ZrO_2 Semiconductor as an Efficient Photocatalyst for Hydrogen Production under UV and Visible Light. *J. Chem. Technol. Biotechnol.* **2017**, *92*, 1503–1510. [CrossRef]

142. Yu, X.; Yang, L.; Xuan, Y.; Liu, X.L.; Zhang, K. Solar−Driven Low−Temperature Reforming of Methanol into Hydrogen via Synergetic Photo− and Thermocatalysis. *Nano Energy* **2021**, *84*, 105953. [CrossRef]
143. Speltini, A.; Scalabrini, A.; Maraschi, F.; Sturini, M.; Pisanu, A.; Malavasi, L.; Profumo, A. Improved Photocatalytic H_2 Production Assisted by Aqueous Glucose Biomass by Oxidized G−C_3N_4. *Int. J. Hydrogen Energy* **2018**, *43*, 14925–14933. [CrossRef]
144. García−López, E.I.; Palmisano, L.; Marcì, G. Overview on Photoreforming of Biomass Aqueous Solutions to Generate H_2 in the Presence of G−C_3N_4−Based Materials. *ChemEngineering* **2023**, *7*, 11. [CrossRef]
145. Zhu, G.; Shu, Y.; Zhou, M. Photocatalytic Conversion of Biomass over Modified Graphitic Carbon Nitride Catalysts for Environmental Sustainability—A Review. *Glob. Environ. Sci.* **2025**, *1*, 19–35. [CrossRef]
146. Jiang, J.; Yu, L.; Peng, J.; Gong, W.; Sun, W. Advance in the Modification of G−C_3N_4−Based Composite for Photocatalytic H_2 Production. *Carbon Lett.* **2025**, *35*, 417–440. [CrossRef]
147. Speltini, A.; Gualco, F.; Maraschi, F.; Sturini, M.; Dondi, D.; Malavasi, L.; Profumo, A. Photocatalytic Hydrogen Evolution Assisted by Aqueous (Waste)Biomass under Simulated Solar Light: Oxidized g−C_3N_4 vs. P25 Titanium Dioxide. *Int. J. Hydrogen Energy* **2019**, *44*, 4072–4078. [CrossRef]
148. Bianchini, P.; Profumo, A.; Cerri, L.; Tedesco, C.; Malavasi, L.; Speltini, A. Exploiting Rice Industry Wastewater for More Sustainable Sunlight−Driven Photocatalytic Hydrogen Production Using a Graphitic Carbon Nitride Polymorph. *RSC Sustain.* **2025**, *3*, 1149–1156. [CrossRef]
149. Lazaar, N.; Wu, S.; Qin, S.; Hamrouni, A.; Bikash Sarma, B.; Doronkin, D.E.; Denisov, N.; Lachheb, H.; Schmuki, P. Single−Atom Catalysts on C_3N_4: Minimizing Single Atom Pt Loading for Maximized Photocatalytic Hydrogen Production Efficiency. *Angew. Chem. Int. Ed.* **2025**, *64*, e202416453. [CrossRef] [PubMed]
150. Hong, Y.; Zhang, X.; Lin, X.; Liu, E.; Wang, L.; Shi, W.; Duan, X. Ultrathin 2D G−C_3N_4 Nanosheets for Visible−Light Photocatalytic Reforming of Cellulose into H_2 under Neutral Conditions. *J. Chem. Technol. Biotechnol.* **2022**, *97*, 1717–1725. [CrossRef]
151. Gao, Y.; Shi, M.; Yang, J.; Wang, Y.; Liu, B. Fabrication of SnS_2/C_3N_5 Heterojunction Photocatalyst for Highly Efficient Hydrogen Production and Organic Pollutant Degradation. *J. Fuel Chem. Technol.* **2025**, *53*, 336–347. [CrossRef]
152. Bu, F.; Yuan, R.; Zhang, Z.; Wang, J.; Liu, J.; Yong, Y.C. Viologen Doping Induced Charge Storage in Carbon Nitride for Enhanced Photocatalytic Hydrogen Production. *Inorg. Chem. Front.* **2024**, *12*, 801–811. [CrossRef]
153. Li, L.; Shi, X.; Liu, L.; Tu, Y.; Liu, Y.; Zhang, Y.; Yang, H.B.; Dou, S.; Liu, B. Modulation of Single−Iron−Atom Coordination Environment toward Three−Electron Oxygen Reduction for Photocatalytic CH_4 Conversion to CH_3OH. *Small* **2025**, *21*, e2500835. [CrossRef]
154. Tahir, M.; Ali Khan, A.; Bafaqeer, A.; Kumar, N.; Siraj, M.; Fatehmulla, A. Highly Stable Photocatalytic Dry and Bi−Reforming of Methane with the Role of a Hole Scavenger for Syngas Production over a Defective Co−Doped g−C_3N_4 Nanotexture. *Catalysts* **2023**, *13*, 1140. [CrossRef]
155. Ali Khan, A.; Tahir, M.; Khan, N. Process Optimization and Kinetic Study for Solar−Driven Photocatalytic Methane Bi−Reforming over TiO_2/Ti_3C_2 Supported CoAlLa−LDH−g−C_3N_4 Dual S−Scheme Nanocomposite. *Energy Convers. Manag.* **2023**, *286*, 117021. [CrossRef]
156. Tasleem, S.; Tahir, M. Constructing $LaxCoyO_3$ Perovskite Anchored 3D G−C_3N_4 Hollow Tube Heterojunction with Proficient Interface Charge Separation for Stimulating Photocatalytic H_2 Production. *Energy Fuels* **2021**, *35*, 9727–9746. [CrossRef]
157. Cheng, T.; Zhu, J.; Chen, C.; Hu, Y.; Wu, L.; Zhang, M.; Cui, L.; Dai, Y.; Zhang, X.; Tian, Y.; et al. Construction of Advanced S−Scheme Heterojunction Interface Composites of Bimetallic Phosphate $MnMgPO_4$ with C_3N_4 Surface with Remarkable Performance in Photocatalytic Hydrogen Production and Pollutant Degradation. *Coatings* **2025**, *15*, 103. [CrossRef]
158. Mohanty, C.; Samal, A.; Kumar, J.; Behera, A.K.; Das, R.; Das, N. Design and First−Principles Investigation of Step−Scheme (S−Scheme) g−$C_3N_4/\alpha-MnO_2$ Nanojunction for Polystyrene Photoreforming into Value−Added Chemicals and Hydrogen. *Int. J. Hydrogen Energy* **2025**, *120*, 628–641. [CrossRef]
159. Ikreedeegh, R.R.; Tahir, M. Facile Fabrication of Well−Designed 2D/2D Porous g−C_3N_4–GO Nanocomposite for Photocatalytic Methane Reforming (DRM) with CO_2 towards Enhanced Syngas Production under Visible Light. *Fuel* **2021**, *305*, 121558. [CrossRef]
160. Xie, Z.K.; Jia, Y.J.; Huang, Y.Y.; Xu, D.B.; Wu, X.J.; Chen, M.; Shi, W.D. Near−Infrared Light−Driven Photocatalytic Reforming Lignocellulose into H_2 and Chemicals over Heterogeneous Carbon Nitride. *ACS Catal.* **2023**, *13*, 13768–13776. [CrossRef]
161. Chung, W.C.; Tsao, I.Y.; Chang, M.B. Novel Plasma Photocatalysis Process for Syngas Generation via Dry Reforming of Methane. *Energy Convers. Manag.* **2018**, *164*, 417–428. [CrossRef]
162. Chung, W.C.; Lee, Y.E.; Chang, M.B. Syngas Production via Plasma Photocatalytic Reforming of Methane with Carbon Dioxide. *Int. J. Hydrogen Energy* **2019**, *44*, 19153–19161. [CrossRef]
163. Iervolino, G.; Vaiano, V.; Sannino, D.; Puga, F.; Navío, J.A.; Hidalgo, M.C. $LaFeO_3$ Modified with Ni for Hydrogen Evolution via Photocatalytic Glucose Reforming in Liquid Phase. *Catalysts* **2021**, *11*, 1558. [CrossRef]
164. Dong, X.; Zhu, X.; Lin, F.; Yan, B.; Li, J.; Chen, G. UV–Vis−Enhanced Photothermal Catalytic Reforming of Biomass Model Tar via $LaMn_xNi_{1-x}O_3$ Perovskite Catalyst. *Chem. Eng. J.* **2023**, *457*, 141112. [CrossRef]

165. Tavasoli, A.; Gouda, A.; Zahringer, T.; Li, Y.F.; Quaid, H.; Viasus Perez, C.J.; Song, R.; Sain, M.; Ozin, G. Enhanced Hybrid Photocatalytic Dry Reforming Using a Phosphated Ni−CeO_2 Nanorod Heterostructure. *Nat. Commun.* **2023**, *14*, 1435. [CrossRef]
166. Balsamo, S.A.; La Greca, E.; Calà Pizzapilo, M.; Sciré, S.; Fiorenza, R. CeO_2−RGO Composites for Photocatalytic H_2 Evolution by Glycerol Photoreforming. *Materials* **2023**, *16*, 747. [CrossRef]
167. Iannaco, M.C.; Mottola, S.; Vaiano, V.; Iervolino, G.; De Marco, I. CeO_2−CuO Composites Prepared via Supercritical Antisolvent Precipitation for Photocatalytic Hydrogen Production from Lactic Acid Aqueous Solution. *J. CO_2 Util.* **2024**, *85*, 102878. [CrossRef]
168. Zhang, Y.; Zhang, M.; Lv, X.; Chen, J.; Jia, H. Maximum Photoresponse in Enhancing Photothermocatalytic Toluene Oxidation: Modulation of Cu^+−Ov−Ce^{3+} and Surface Lattice Oxygen via Cu/CeO_2 Shape Effect. *Appl. Catal. B Environ.* **2025**, *371*, 125253. [CrossRef]
169. Aoun, N.; García−López, E.I.; Boucheloukh, H.; Boulekroune, M.; Sehili, T.; Marcì, G. $SrNiO_3$ Perovskite/CeO_2 Composites as Heterogeneous Photocatalysts for the 2−Propanol Oxidation in Gas–Solid Regime. *J. Photochem. Photobiol. A Chem.* **2025**, *458*, 115930. [CrossRef]
170. Li, A.; Ma, J.; Hong, M.; Sun, R. Enhanced CeO_2 Oxygen Defects Decorated with $AgInS_2$ Quantum Dots Form an S−Scheme Heterojunction for Efficient Photocatalytic Selective Oxidation of Xylose. *Appl. Catal. B Environ.* **2024**, *348*, 123834. [CrossRef]
171. Wang, Z.; Wang, Q.; Yin, Z.; Zhang, M.; Yu, G.; Luo, Q.; Chen, H.; Tang, B.; Li, K.; Zhang, Z.; et al. Non−Noble CeO_2/CdS/NiS Heterojunction for Photoredox−Catalyzed Plastic Waste Selective Synthesis and Hydrogen Production from Natural Seawater. *Fuel* **2025**, *385*, 134143. [CrossRef]
172. Li, T.; Guo, X.; Zhang, L.; Yan, T.; Jin, Z. 2D CoP Supported 0D WO_3 Constructed S−Scheme for Efficient Photocatalytic Hydrogen Evolution. *Int. J. Hydrogen Energy* **2021**, *46*, 20560–20572. [CrossRef]
173. Wang, H.; Xiao, M.; Wang, Z.; Chen, X.; Dai, W.; Fu, X. Visible Photocatalytic Hydrogen Production from CH_3OH over CuO/WO_3: The Effect of Electron Transfer Behavior of the Adsorbed CH_3OH. *Chem. Eng. J.* **2023**, *459*, 141616. [CrossRef]
174. Alaoui, C.; Karmaoui, M.; Bekka, A.; Edelmannova, M.F.; Gallardo, J.J.; Navas, J.; Touati, W.; Kadi Allah, I.; Figueiredo, B.; Labrincha, J.A.; et al. TiO_2/WO_3/Graphene for Photocatalytic H_2 Generation and Benzene Removal: Widely Employed Still an Ambiguous System. *J. Photochem. Photobiol. A Chem.* **2023**, *445*, 115020. [CrossRef]
175. Albukhari, S.M.; Al−Hajji, L.A.; Ismail, A.A. Construction of N−n Heterojunction Copper Manganese Spinel/Mesoporous WO_3 Photocatalyst for Efficient H_2 Evolution Rate from Aqueous Glycerol. *Renew. Energy* **2024**, *228*, 120649. [CrossRef]
176. Ye, X.; Dong, Y.; Zhang, Z.; Zeng, W.; Zhu, B.; Zhang, T.; Gao, Z.; Dai, A.; Guan, X. Syngas Production by Photoreforming of Formic Acid with 2D $V_xW_{1-x}N_{1.5}$ Solid Solution as an Efficient Cocatalyst. *Front. Energy* **2024**, *18*, 640–649. [CrossRef]
177. Zhou, C.; Wu, J.; Li, Y.; Cao, H. Highly Efficient UV−Visible−Infrared Light−Driven Photothermocatalytic Steam Biomass Reforming to H_2 on Ni Nanoparticles Loaded on Mesoporous Silica. *Energy Environ. Sci.* **2022**, *15*, 3041–3050. [CrossRef]
178. Zhong, M.; Li, Y.; Wu, J.; Hu, Q.; Hu, Y.; Du, Q.; Ji, C.; Cao, H.; Ji, L. Light Promotion and Different Reaction Pathways Enhance Photothermocatalytic Syngas Production for Cellulose Steam Reforming over Ni/θ−Al_2O_3. *Adv. Funct. Mater* **2024**, *34*, 2405453. [CrossRef]
179. Levenspiel, O. Chapter 19—The Packed Bed Catalytic Reactor. In *Chemical Reaction Engineering*; Levenspiel, O., Ed.; John Wiley & Sons: Hoboken, NJ, USA, 1998; Volume 1, ISBN 978-0-471-25424-9.
180. Liu, L.; Li, Y.; He, J.; Wang, Q.; Deng, J.; Chen, X.; Yu, C. Progress on Gas−Solid Phase Photoreactor and Its Application in CO_2 Reduction. *Green Chem. Eng.* **2024**, *5*, 290–306. [CrossRef]
181. Kim, S.; Kim, S.; Park, H.-J.; Park, S.; Kim, J.Y.; Jeong, Y.W.; Yang, H.H.; Choi, Y.; Yeom, M.; Song, D.; et al. Practical Scale Evaluation of a Photocatalytic Air Purifier Equipped with a Titania−Zeolite Composite Bead Filter for VOC Removal and Viral Inactivation. *Environ. Res.* **2022**, *204*, 112036. [CrossRef]
182. Nguyen, T.-V.; Wu, J.C.S. Photoreduction of CO_2 to Fuels under Sunlight Using Optical−Fiber Reactor. *Sol. Energy Mater. Sol. Cells* **2008**, *92*, 864–872. [CrossRef]
183. Tong, K.; Chen, L.; Yang, L.; Du, X.; Yang, Y. Energy Transport of Photocatalytic Carbon Dioxide Reduction in Optical Fiber Honeycomb Reactor Coupled with Trough Concentrated Solar Power. *Catalysts* **2021**, *11*, 829. [CrossRef]
184. Kunii, D.; Levenspiel, O. Chapter 1—Introduction. In *Fluidization Engineering*; Butterworth−Heinemann; Elsevier: Newton, MA, USA, 1991; Volume 1, pp. 1–13.
185. Lee, J.K.; Park, D. Hydrogen Production from Fluidized Bed Steam Reforming of Hydrocarbons. *Korean J. Chem. Eng.* **1998**, *15*, 658–662. [CrossRef]
186. Zambrano, D.; Soler, J.; Herguido, J.; Menéndez, M. Conventional and Improved Fluidized Bed Reactors for Dry Reforming of Methane: Mathematical Models. *Chem. Eng. J.* **2020**, *393*, 124775. [CrossRef]
187. Zheng, H.; Jiang, X.; Gao, Y.; Tong, A.; Zeng, L. Chemical Looping Reforming: Process Fundamentals and Oxygen Carriers. *Discov. Chem. Eng.* **2022**, *2*, 5. [CrossRef]
188. Gusmão, C.; Palharim, P.H.; Diniz, L.A.; de Assis, G.C.; de Carvalho e Souza, T.; Ramos, B.; Teixeira, A.C.S.C. Advances in Fluidized Bed Photocatalysis: Bridging Gaps, Standardizing Metrics, and Shaping Sustainable Solutions for Environmental Challenges. *Ind. Eng. Chem. Res.* **2024**, *63*, 14967–14982. [CrossRef]

189. Rincón, G.J.; La Motta, E.J. A Fluidized−Bed Reactor for the Photocatalytic Mineralization of Phenol on TiO_2−Coated Silica Gel. *Heliyon* **2019**, *5*, e01966. [CrossRef]
190. Prieto, O.; Fermoso, J.; Irusta, R. Photocatalytic Degradation of Toluene in Air Using a Fluidized Bed Photoreactor. *Int. J. Photoenergy* **2007**, *2007*, 032859. [CrossRef]
191. Vaiano, V.; Sannino, D.; Ciambelli, P. Steam Reduction of CO_2 in a Photocatalytic Fluidized Bed Reactor. *Chem. Eng. Trans.* **2015**, *43*, 1003–1008. [CrossRef]
192. Costa, A.L.; Ortelli, S.; Blosi, M.; Albonetti, S.; Vaccari, A.; Dondi, M. TiO_2 Based Photocatalytic Coatings: From Nanostructure to Functional Properties. *Chem. Eng. J.* **2013**, *225*, 880–886. [CrossRef]
193. Kunii, D. Levenspiel Octave Chapter 3—Fluidization and Mapping of Regimes. In *Fluidization Engineering*; Butterworth−Heinemann; Elsevier: Newton, MA, USA, 1991; Volume 1, pp. 61–94, ISBN 978-0-08-050664-7.
194. Ammendola, P.; Chirone, R. Aeration and Mixing Behaviours of Nano−Sized Powders under Sound Vibration. *Powder Technol.* **2010**, *201*, 49–56. [CrossRef]
195. Zhang, Q.; Liu, W.; Cao, Y.; Gai, H.; Zhu, Q. Diverse Gas−Solid Magnetized Fluidized Beds with Different Magnetic Fields. *Powder Technol.* **2024**, *433*, 119241. [CrossRef]
196. Ruoppolo, G.; Miccio, F.; Chirone, R. Fluidized Bed Cogasification of Wood and Coal Adopting Primary Catalytic Method for Tar Abatement. *Energy Fuels* **2010**, *24*, 2034–2041. [CrossRef]
197. Xiong, H.; Dong, Y.; Liu, D.; Long, R.; Kong, T.; Xiong, Y. Recent Advances in Porous Materials for Photocatalytic CO_2 Reduction. *J. Phys. Chem. Lett.* **2022**, *13*, 1272–1282. [CrossRef]
198. Miccio, F.; Boscherini, M.; Minelli, M.; Doghieri, F. A Comparative Investigation on Mixing and Dispersion in Fluidized Bed Equipped with a Conical Distributor for Catalytic Processes. *J. Ind. Eng. Chem.* 2025, *preprint*. [CrossRef]
199. Rizzuti, L.; Yue, P.L. The Measurement of Light Transmission through an Irradiated Fluidised Bed. *Chem. Eng. Sci.* **1983**, *38*, 1241–1249. [CrossRef]
200. Braham, R.J.; Harris, A.T. A Complete Multi−Scale Simulation of Light Absorption within a Fluidized Bed Photoreactor Using Integrated Particle, Fluid and Photon Behaviour Models. *Phys. Chem. Chem. Phys.* **2013**, *15*, 12373. [CrossRef]
201. Svoboda, K.; Kalisz, S.; Miccio, F.; Wieczorek, K.; Pohořelý, M. Simplified Modeling of Circulating Flow of Solids between a Fluidized Bed and a Vertical Pneumatic Transport Tube Reactor Connected by Orifices. *Powder Technol.* **2009**, *192*, 65–73. [CrossRef]
202. Lolli, A.; Blosi, M.; Ortelli, S.; Costa, A.L.; Zanoni, I.; Bonincontro, D.; Carella, F.; Albonetti, S. Innovative Synthesis of Nanostructured Composite Materials by a Spray−Freeze Drying Process: Efficient Catalysts and Photocatalysts Preparation. *Catal. Today* **2019**, *334*, 193–202. [CrossRef]
203. Tran, A.; Aguirre, A.; Durand, H.; Crose, M.; Christofides, P.D. CFD Modeling of a Industrial−Scale Steam Methane Reforming Furnace. *Chem. Eng. Sci.* **2017**, *171*, 576–598. [CrossRef]
204. Garland, J.R.; van Helmond, P. Steam Reformer Tube Assembly and Method of Assembling or Retrofitting Same. U.S. Patent 8,776,344B2, 15 July 2014.
205. Fonseca, J.D.; Camargo, M.; Commenge, J.-M.; Falk, L.; Gil, I.D. Trends in Design of Distributed Energy Systems Using Hydrogen as Energy Vector: A Systematic Literature Review. *Int. J. Hydrogen Energy* **2019**, *44*, 9486–9504. [CrossRef]
206. Jaison, A.; Mohan, A.; Lee, Y.-C. Machine Learning−Enhanced Photocatalysis for Environmental Sustainability: Integration and Applications. *Mater. Sci. Eng. R Rep.* **2024**, *161*, 100880. [CrossRef]
207. Mowbray, M.; Vallerio, M.; Perez−Galvan, C.; Zhang, D.; Del Rio Chanona, A.; Navarro−Brull, F.J. Industrial Data Science—A Review of Machine Learning Applications for Chemical and Process Industries. *React. Chem. Eng.* **2022**, *7*, 1471–1509. [CrossRef]